SERI/STR-211-2861
DE86004420

January 1986

Research on High-Efficiency, Single-Junction, Monolithic, Thin-Film Amorphous Silicon Solar Cells

Semiannual Subcontract Progress Report
1 December 1984 - 31 May 1985

G.R. Ashton
F.E. Aspen
R.L. Jacobson
F.R. Jeffrey
N.T. Tran
Electronic and Information Sector
Laboratories/3M

Prepared under Subcontract No. ZB-4-03056-2

SERI

Solar Energy Research Institute
A Division of Midwest Research Institute

1617 Cole Boulevard
Golden, Colorado 80401-3393

Operated for the
U.S. Department of Energy
under Contract No. DE-AC02-83CH10093

SERI/STR-211-2861
UC Category: 63
DE86004420

Research on High-Efficiency, Single-Junction, Monolithic, Thin-Film Amorphous Silicon Solar Cells

Semiannual Subcontract Progress Report 1 December 1984 - 31 May 1985

G.R. Ashton
F.E. Aspen
R.L. Jacobson
E.R. Jeffrey
N.T. Tran

Electronic and Information Sector
Laboratories/3M

January 1986

SERI Technical Monitor:
W. Wallace

Prepared under Subcontract No. ZB-4-03056-2

Solar Energy Research Institute
A Division of Midwest Research Institute

1617 Cole Boulevard
Golden, Colorado 80401-3393

Prepared for the
U.S. Department of Energy
Contract No. DE-AC02-83CH10093

PREFACE

This Semi-Annual Report covers the work performed by the Electrical and Communications Technologies Laboratory of the 3M Company, St. Paul, Minnesota, for the period 01 December 1984 to 31 May 1985 under Subcontract No. ZB-4-03056-2. The Project Manager is Dr. Donald L. Janes and the Technical Manager is Dr. James V. Burt. The staff members (and associate staff personnel) who have contributed to the report, and their areas of specialization, are listed below.

Dr. Gary R. Ashton	Research Specialist, Submodule Design/Fabrication Task Four Leader
Dr. Frank E. Aspen	Research Specialist, Sputter Deposition of Thin Films Task Two Leader
Dr. Fred Bacon	Surface Analysis
Mr. Joseph Cross	Solar Simulator
Mr. John K. Echo	Graphic Design
Mr. Jathan Edwards	Amorphous Silicon Deposition
Dr. Kenneth A. Epstein	Transport and Stability Measurements
Dr. Derrick Grimmer	Stability Measurements
Dr. Erick Hockert	Laser Scribing
Mr. Richard L. Jacobson	Senior Research Specialist, Multi-Chamber Vacuum System Design/Fabrication Task Five Leader
Dr. Frank R. Jeffrey	Research Specialist, Amorphous Silicon Device Fabrication/Measurement Task Three Leader
Mr. David C. Knoll	Laser Scanner for Defects
Mr. Pat Lasswell	University of Delaware, Institute of Energy Conversion Laser Scanner
Dr. Dave Misemer	Device Modeling
Dr. Arnold Moore	University of Delaware, Institute of Energy Conversion Surface Photovoltage

Mr. David J. Mullen	Technical Report Editor
Mr. David V. Nins	ITO Deposition
Mr. Donald J. Olsen	Amorphous Silicon Deposition
Dr. Rajendra I. Patel	Plasma Diagnostics
Dr. Thomas C. Paulick	Optical Modeling for Back Contact
Mr. Ken Paulson	Laser Scribing
Mr. James Petrell	Computer Control
Dr. James Phillips	University of Delaware, Institute of Energy Conversion Solar Simulation
Ms. Joan Richards	Laser Scribing
Ms. Christine Swansen	Gas Purity Analysis
Ms. Linda S. Thalhuber	Government Programs Coordinator
Dr. Nang Tran	Research Specialist, Amorphous Silicon Material Deposition Measurement Task One Leader
Mr. George D. Vernstom	Amorphous Silicon Deposition and Measurement
Dr. Michael Weber	Amorphous Silicon Deposition
Mr. Roger K. Westerberg	Mechanical Design Engineer
Mr. Robert C. Williams	Amorphous Silicon Deposition
Mr. Steve Znameroski	Metallization

SUMMARY

Development of technology and systems capabilities to facilitate continuous, large-area deposition onto flexible substrates is critically important for successful commercialization of thin film a-Si solar cells. This capability will minimize two major factors influencing the overall manufacturing cost of amorphous silicon photovoltaic devices--capital costs and substrate handling costs. Capital costs are minimized by utilizing systems which operate continuously, and substrate handling costs are minimized by maximizing the substrate size.

3M is in a unique position to make significant contributions to advance the state-of-the-art in thin-film amorphous silicon solar cell development through the efforts being made in this contract as well as in similar areas of expertise which utilize continuous, large-area deposition techniques on flexible substrates. Prior to the initiation of this contract, 3M had demonstrated the capability of depositing large areas of a-Si:H on polyimide roll material for other applications.

Deposition System One has been modified and is now capable of simultaneously depositing films on eight substrates per run. Depositions are monitored by plasma diagnostics using both optical emission and quadrupole mass spectroscopy.

A diffusion length of 0.57 micrometer for AM1 illumination was achieved for intrinsic a-Si deposited on metal-coated polyimide substrate.

Modifications to the gas analysis system will allow detection levels of approximately 1 ppm. Deposition rates of 12 Å/second for pure silane and 8 Å/second for a mixture of silane/hydrogen or silane/helium have been achieved. A source of high purity Si_2H_6 gas has been identified and efforts to achieve higher deposition rates using silane in System One, are in progress.

Stability studies were initiated by lightly doping intrinsic layers with boron, fluorine, boron and fluorine, and by compensating phosphorous with boron. Stress, electron spin resonance, photocurrent, surface photovoltage, time-of-flight and photoluminescence measurements will be used to study degradation mechanisms.

Evaluation of the thermal, mechanical, and physical properties of polyimide film from four vendors is discussed in Section 3.0.

Either Ni or Al will be chosen for use as the back metal contact. If Al is chosen, a diffusion barrier at the Al/a-Si interface will be required. Although stainless steel is an effective diffusion barrier for Al, it will not be used due to its low reflectivity.

Indium tin oxide (ITO) is used for the front contact. When deposited at room ambient, a 2100 $\mathring{A}$ thick ITO film has a sheet resistance of 35 ohms/square with a 2-5% absorption loss over wavelengths of 500 to 700 nanometers. Heat treatment studies at 130^{o}C indicate that the ITO/a-Si interface is unstable, even at moderate temperatures. A diffusion barrier is also needed at this interface.

An investigation to characterize defects in a-Si devices is progressing. EBIC is used to study the types as well as the densities of defects in photovoltaic devices fabricated on polyimide substrates. The four major categories of defects are discussed in Section 4.0 of this report.

The effect of substrate surface roughness on the charge collection of a-Si devices and the relationship between active area and defect density will be addressed in subsequent studies.

The thermal coefficient of expansion of our best polyimide film and of a-Si are very similar, which significantly reduces web curling after deposition. By reducing the formation of Si powder accumulations in System 4, a marked improvement in device quality has been realized.

Intrinsic layer doping with boron in single chamber systems is ineffective due to the extensive level of boron carry-over from depositing the p^+ layer. In the new two chamber system an improved p^+-i interface and a reduction of the boron content in the i-layer have been demonstrated.

Construction of monolithic a-Si solar cell submodules was achieved using series connected 0.5 x 10.0 centimeter cells fabricated on flexible polyimide substrate. A YAG laser has been successfully used to produce the three types of cuts necessary to electrically connect the cells in series. These laser scribing steps require accurate substrate positioning and laser output control.

A solar simulator using ELH bulbs has been constructed for solar simulation testing over a 10 x 10 centimeter area. Reference cells calibrated at SERI are used to establish standard test conditions in this solar simulator. Defect detection using a laser scanner has been performed on 3M's solar cells. Evaluation of the submodules for defects and efficiency is a continuing effort.

The multi-chamber deposition system for depositing a-Si onto polyimide flexible web is essentially complete. The vacuum chambers have been helium leak-checked, and a base pressure of 10^{-6} torr was routinely obtained during initial tests. Two pumping systems are attached to the large chamber. One is a high vacuum system consisting of a 450 liter/second turbomolecular pump backed by a 30 cfm rotary vane pump to evacuate the multi-chamber to a low base pressure prior to deposition runs. The second system consists of a WA 1000 roots blower backed by a DK 200 rotary piston pump to pump process gases during deposition runs.

The amorphous silicon solar cell research program is proceeding on schedule and 3M is very optimistic that all future objectives, performance milestones and program deliverables associated with this contract will be successfully accomplished.

TABLE OF CONTENTS

LIST OF FIGURES

LIST OF TABLES

LIST OF EQUATIONS

1.0 INTRODUCTION

The present program, which is entitled: "Research On High Efficiency Single-Junction Monolithic Thin Film Amorphous Silicon Solar Cells," consists of five research tasks. These tasks are: (1) amorphous silicon materials research, (2) non-semiconductor materials research, (3) solar cell research, (4) monolithic, intra-connected cells/submodule research and (5) multi-chamber deposition system research.

2.0 TASK ONE - AMORPHOUS SILICON MATERIALS RESEARCH

2.1 Measurement Facilities

The facilities required to characterize the basic a-Si materials are listed in Table 2-1.

Table 2-1. Measurement Facilities

Measurement	Facility/System
Activation Energy	Dedicated computer-controlled facility to measure temperature dependent conductivity from -20°C to +130°C
Photoconductivity	Manual instruments, white and monochromatic illumination
Optical Absorption	Dedicated Varian 2300 spectrophotometer
Infrared Transmission	Facilities within 3M Central Research Laboratories, and a similar system in 3M Analytical Department.
Auger Analysis	Facilities within 3M Electronics and Information Sector Research Laboratory (E&I Sector Laboratory)
SIMS Analysis	SIMS units available in a Division Lab
Surface Photovoltage	Fully automated system, constructed at the University of Delaware, is in-house
C-V Measurements	Dedicated computerized facility
I-V Measurements	Computerized system with ELH illumination
Raman Scattering	In-house system with laser illumination. Access to similar system in 3M Analytical Department
Photoluminescence	Facilities within 3M E&I Sector Laboratory
Time-of-flight measurements	Facilities within 3M E&I Sector Laboratory
ESR	Facilities within 3M E&I Sector Laboratory
ESCA	Facilities within 3M E&I Sector Laboratory
Stress Measurements	System currently under construction

2.2 Amorphous Silicon Materials Research Progress

2.2.1 Gas Analysis by Mass Spectroscopy

Our laboratory has built a dedicated system for analyzing the purity of gases used in the deposition of a-Si. The system is based on the method of analysis known as "modulated beam mass spectrometry." Test gas from a cylinder being analyzed is metered into a vacuum system and a gas beam is defined by a limiting aperture. To minimize the effect of residual background gases, the beam is mechanically chopped just prior to entering the ionization section of the mass spectrometer. Measurements are performed using a UTI quadrupole spectrometer, Model 100C, with a mass range to 300 AMU. The quadrupole output approximates a square wave and is measured using a Princeton Model 5101 lock-in amplifier. The dc output as a function of mass/charge is displayed on an X-Y recorder. In this manner, spectra are generated which are relatively free of background peaks.

An earlier gas analysis system had Viton O-rings and was pumped by a Leybold-Heraeus TMP 450 liter/second turbomolecular pump. A base pressure of approximately 1×10^{-8} torr was achievable in an aluminum chamber. A detection sensitivity of approximately 5 ppm was typical when operating at an electron emission current of 0.5 mA. Greater sensitivity could be realized at higher currents, however, interference peaks from residual gases (primarily water vapor, nitrogen, and oxygen) became more evident. These interference peaks were 180° out of phase with the gas beam peaks, thus driving the chart recorder below its zero line. These negative peaks obscured those originating from the gas beam.

Our new gas analysis system employs a stainless steel chamber and Conflat copper gaskets. This system is pumped with a TMP 360 liter/second turbomolecular pump, and both the system and the pump can be baked. This system should be capable of reaching a base pressure in the range of 10^{-10} torr. Presently, pressures in the range of 10^{-9} torr have been achieved without baking. This system is expected to provide detection sensitivities of approximately 1 ppm when operated at higher electron emission currents (2 to 3 mA).

With the earlier gas analysis system, test results generally indicated that the majority of incoming cylinders contained essentially pure gas at the detection limit of 5 to 10 ppm. These positive results are believed to have been the result of procedures which were established to minimize contamination from the gas manifold. The gas manifold is routinely leak checked with helium and usually degassed under high vacuum prior to testing. In addition, the manifold is thoroughly flushed with gas from the cylinder to be tested prior to performing mass spectra measurements. Even with these precautions, a small amount (< 100 ppm) of argon is frequently observed in the spectra. It is believed that argon originates from the argon purge cycle which is used when changing cylinders. The manifold contains several Teflon coated NPT fittings which apparently outgas argon for long periods of time. Plans are to replace these Teflon fittings with VCR fittings in the near future.

In gas analyses in which contaminates have been observed, 10 to 20 ppm levels of oxysilane have been detected in several completely used cylinders of silane and 1% of methylsilane was present in one disilane cylinder. Monosilane cylinders typically exhibit higher order silanes at levels of less than 1%. These levels probably have little or no significant effect on the properties of a-Si films.

2.2.2 Intrinsic Material

A new reactor design has been incorporated into deposition System One. The dimensions of this reactor are the same as those of Systems Three and Four in order to maintain a consistent geometry relationship with the other systems as shown in Figure 2-1. Several series of depositions have been performed in Systems One and Two in order to determine the optimum parameters for depositing intrinsic material. Parameters which were studied included: a) varying the RF power and SiH_4 flow rate, b) heating the substrate to 250^{o}C, c) using a system pressure of 1 torr, and d) varying the ratios of SiH_4/H_2 and SiH_4/He.

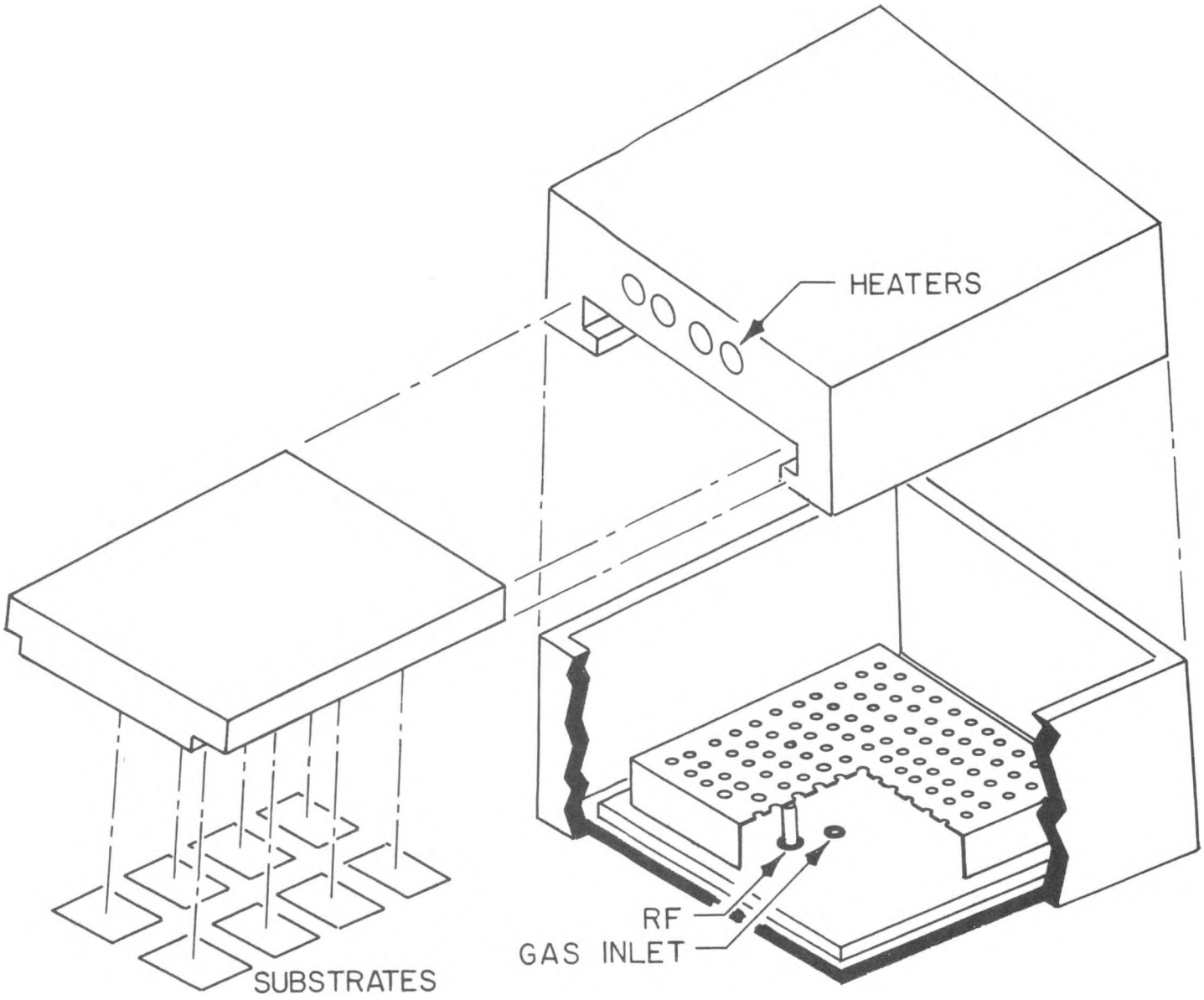

Figure 2-1. Schematic Diagram Of The Reactor For System One

2.2.2.1 High Deposition Rate of Intrinsic Material

In studying the high deposition rate of intrinsic layers, runs were performed using various SiH_4/H_2 gas mixtures. A variety of SiH_4/He gas mixtures were used in order to establish additional baseline information before attempting to perform depositions with Si_2H_6/He mixtures. Gas analysis results for a mixture of 10% silane in hydrogen are shown in Figure 2-2. The species H^+, H_2^+, H_3^+, SiH_x^+ and $Si_2H_x^+$ were observed.

Gas analysis results for pure SiH_4 and pure He are shown in Figures 2-3 and 2-4, respectively. SiH_x^+ and $Si_2H_x^+$ peaks were observed. $Si_2OH_x^+$ was also observed in some of the cylinders tested. A cylinder containing helium gas showed an additional peak at m/e equal to 20. This is believed to be neon.

Improvement of the deposition rate is important in order to make continuous processing of flexible a-Si solar cells economical. High deposition rate studies were performed in System One prior to system modifications. Although non-uniformity and reproducibility problems existed in the system, generally, a deposition rate of 12 Å/sec for pure silane, and 8 Å/sec for a mixture of silane/hydrogen or silane/helium was attained as shown in Figure 2-5. Helium, as compared to hydrogen, at a given deposition condition, was observed to exhibit: a) less dusting, and b) greater plasma stability. The electrical and optical properties of undoped silicon films produced with either silane mixture are very similar.

High deposition rate studies, using SiH_4/He and SiH_4/H_2 mixtures in deposition System One, are continuing.

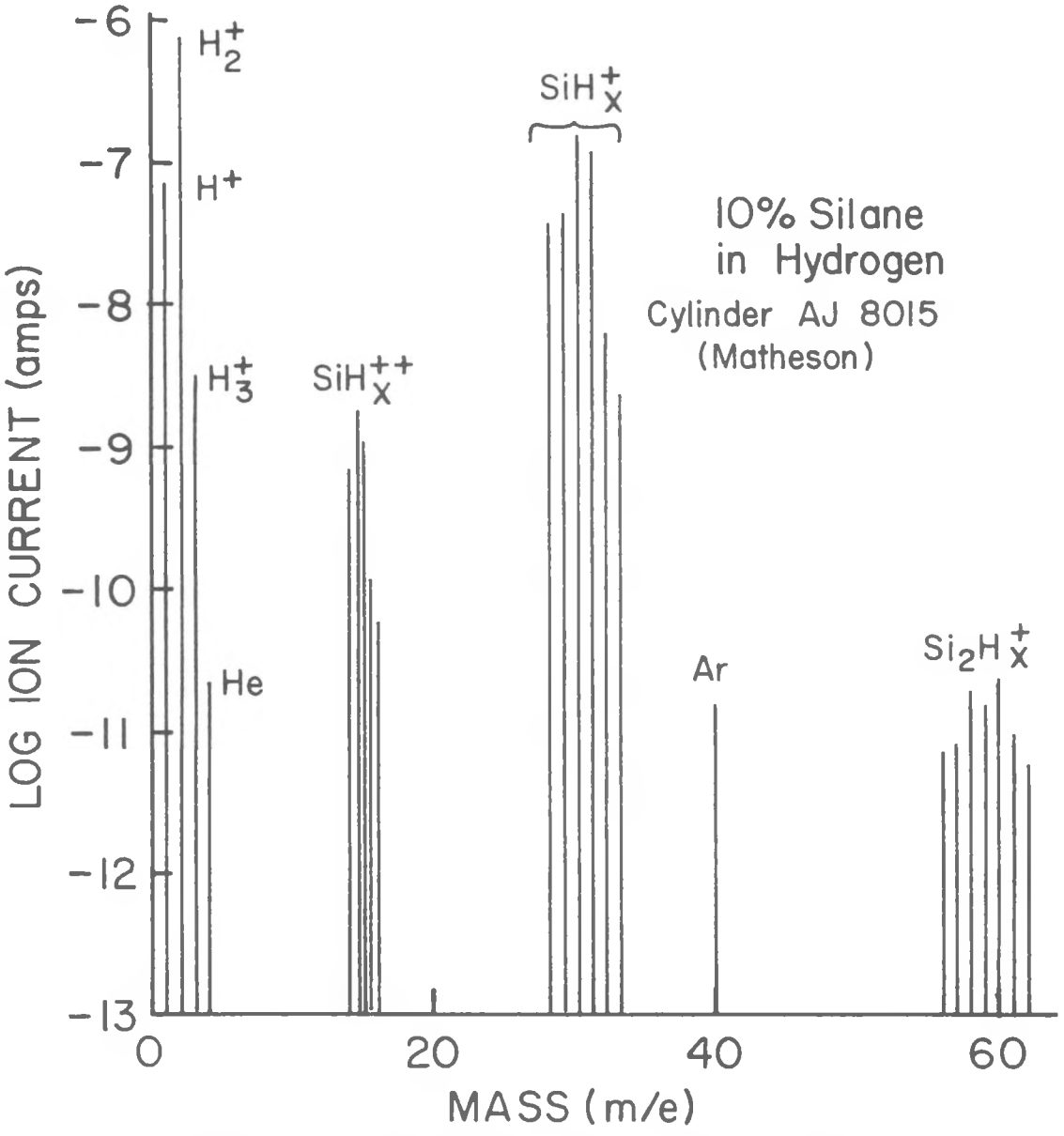

Figure 2-2. Mass Spectra Of 10% Silane In Hydrogen

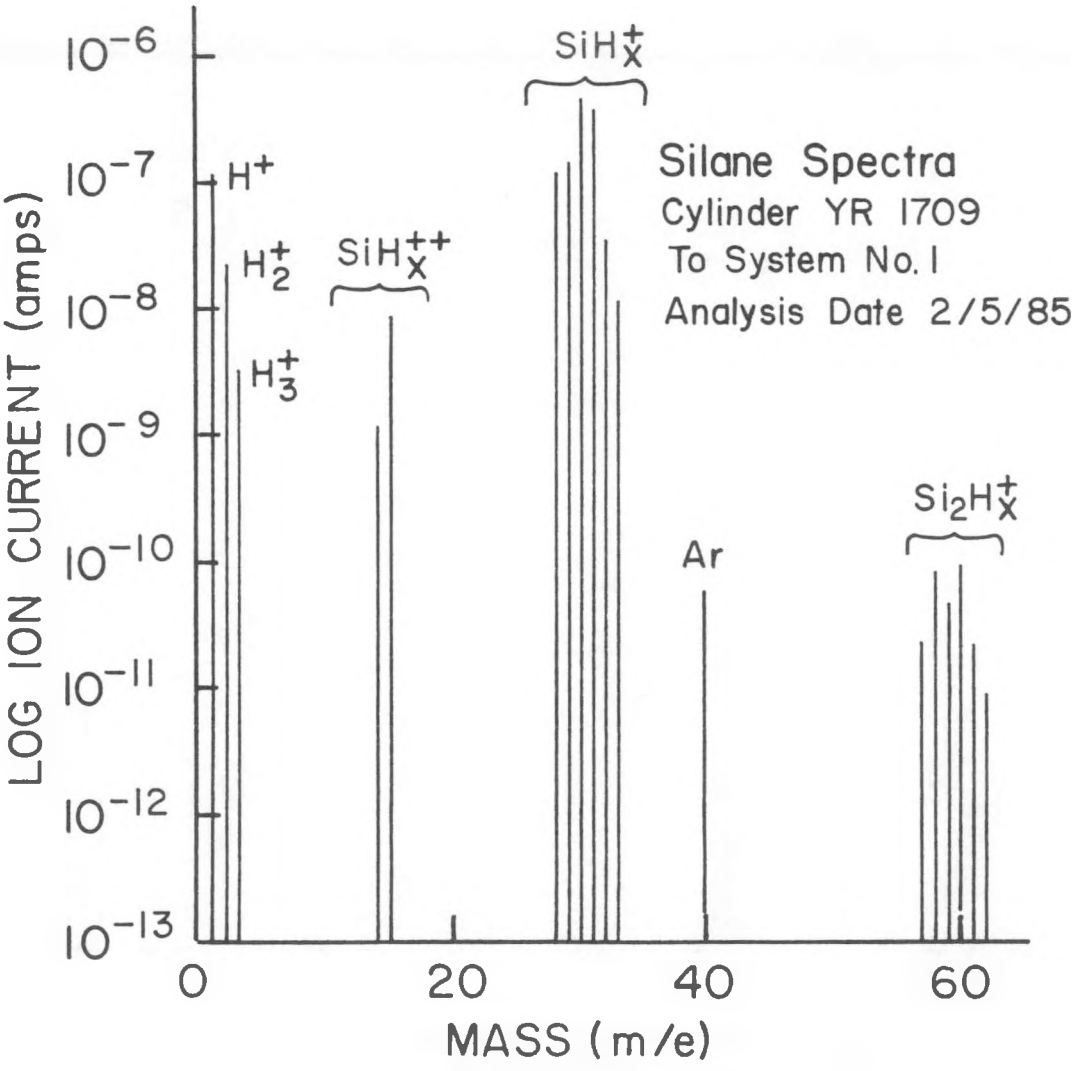

Figure 2-3. Mass Spectra Of Pure Silane

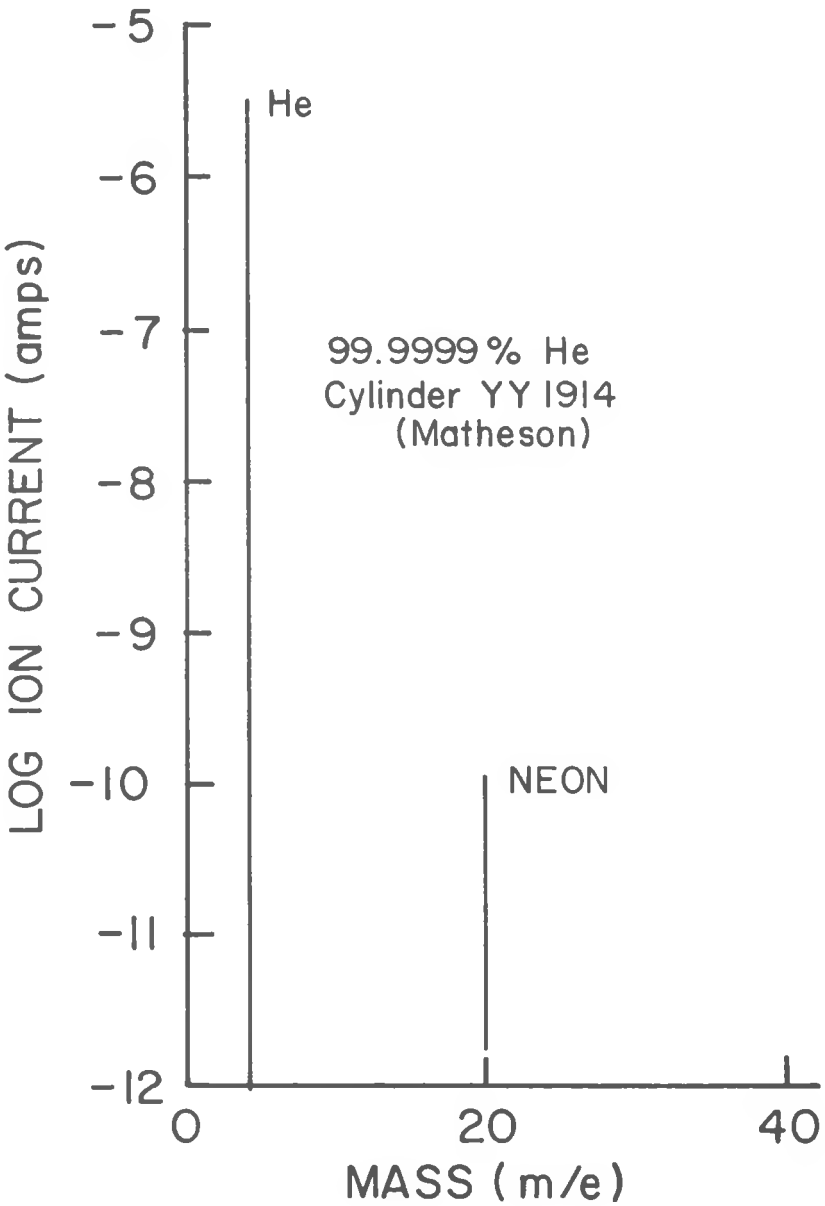

Figure 2-4. Mass Spectra Of Pure Helium

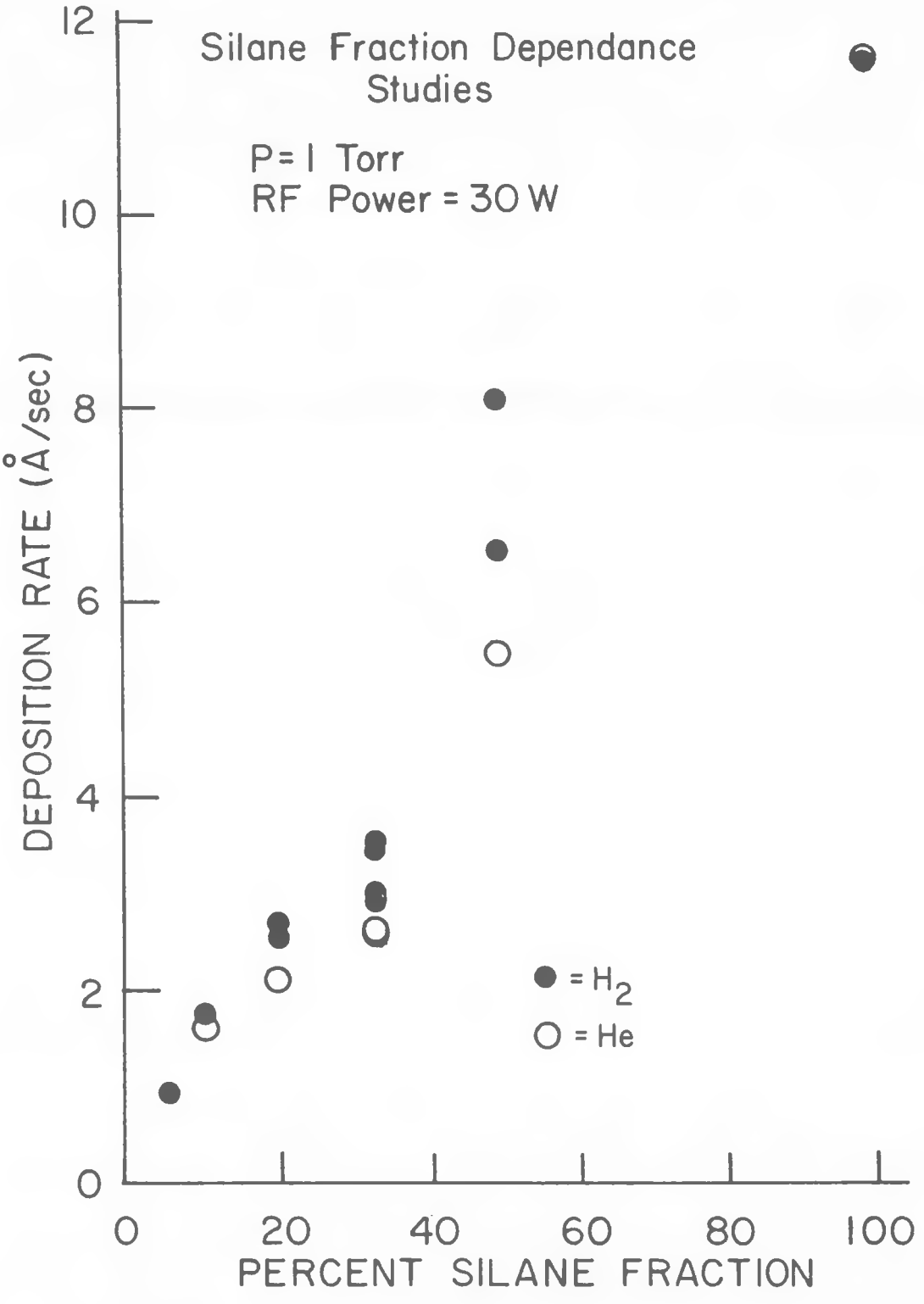

Figure 2-5. Variation Of Deposition Rate As A Function Of Silane Fraction In H_2 And He

2.2.2.2 Diffusion Length

A computerized system for measuring surface photovoltage was designed and built by Dr. Arnold Moore of the Institute of Energy Conversion at the University of Delaware. A schematic diagram of the system is shown in Figure 2-6. The quinone-hydroquinone electrolyte is contained in an O-ring gasketed cell which allows light to reach the a-Si films while permitting easy sample interchange. An HP 3497A data acquisition system and HP 86B controller disk drive are used to store and print data. References 1 and 2, provide additional detailed information.

Two drawbacks with the surface photovoltage technique are: a) obtaining accurate absorption coefficients beyond 10^4 cm^{-1}, and b) the diffusion length depends on the curve fitting routine. A program for determining n and k was written, and accurate absorption coefficient data is now obtainable.

A diffusion length of 0.57 microns for AM1 illumination was established for intrinsic a-Si films deposited on metallized polyimide substrate is shown in Figure 2-7. This value exceeds the milestone value established by SERI for diffusion length in metal-coated polyimide substrate. Polarity inversion was observed in boron-doped samples. The mechanism for this phenomena is being investigated.

A study involving light-induced effects on the diffusion length is progressing.

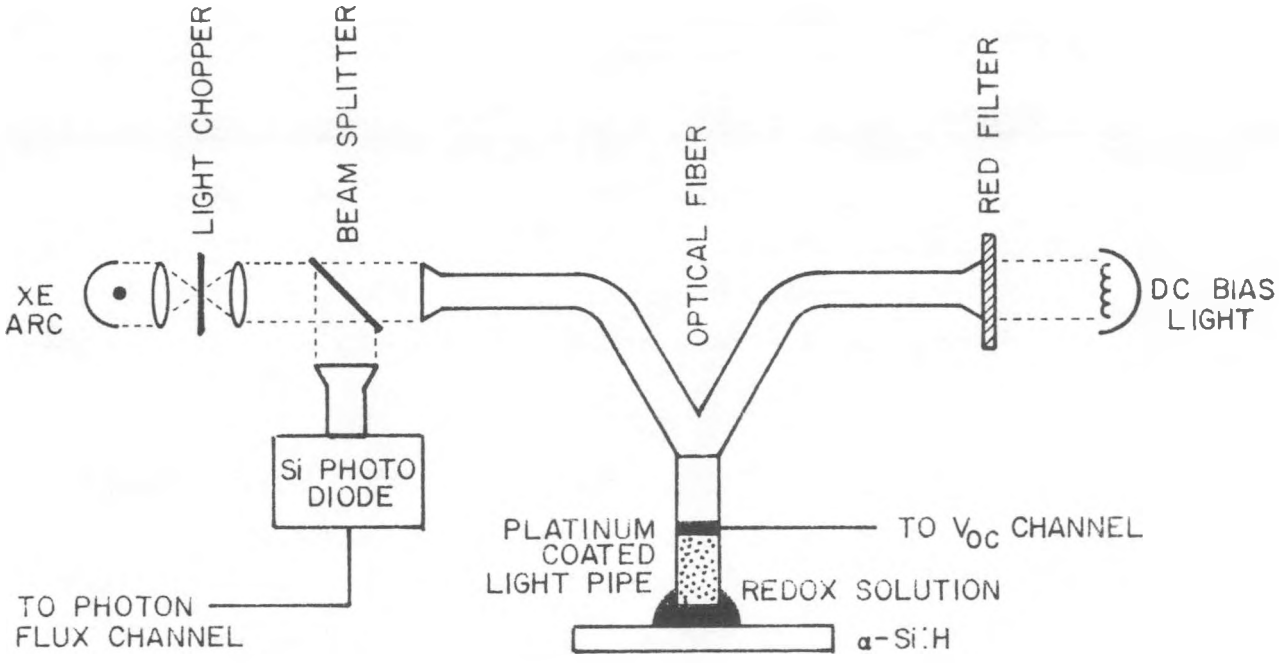

Figure 2-6. Block Diagram Of SPV Apparatus Using Redox Electrochemical Liquid Pickup
Light is conducted to the sample surface by fiber optics. A servo loop adjusts the light intensity to keep the SPV constant at all wavelengths.

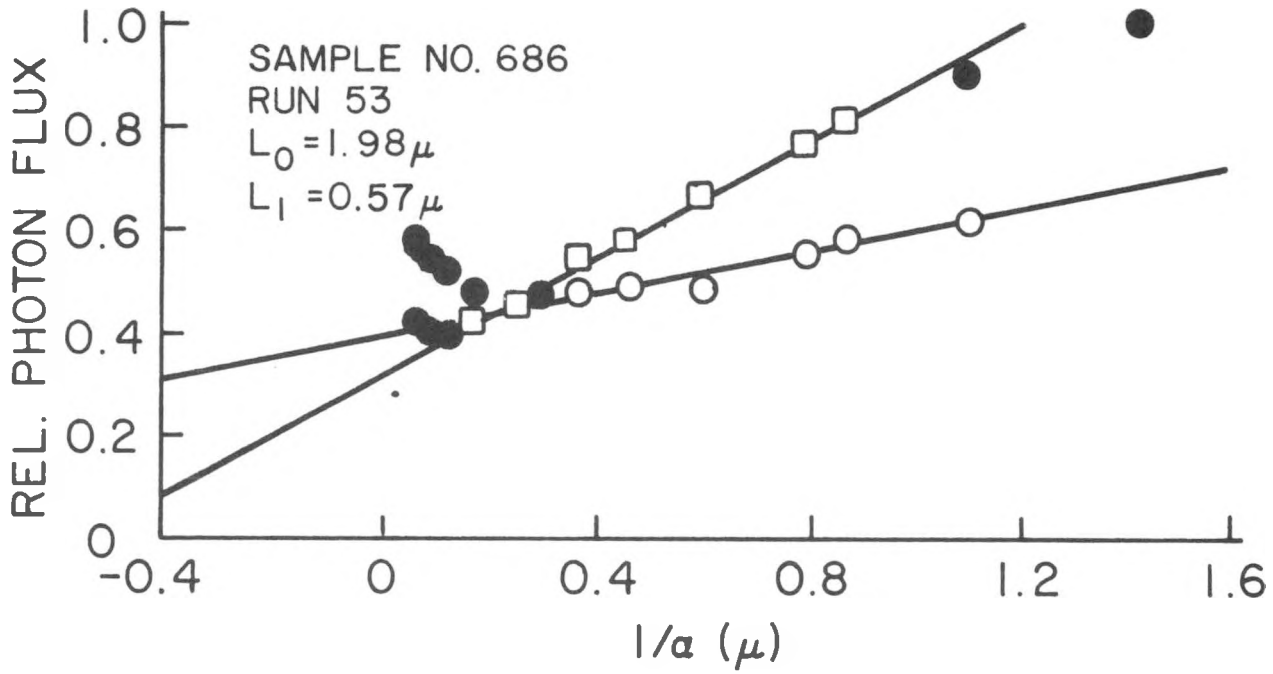

Figure 2-7. A Diffusion Length Of 0.57 Micron Was Obtained In Amorphous Silicon Films On Metal Coated Polyimide Substrate

2.2.3 Plasma Diagnostics

2.2.3.1 Thermodynamic Study of the Silane-Hydrogen Chemical System

Thermodynamic calculations of the chemical equilibrium compositions of various species were performed for the silane/hydrogen system at different temperatures (500-6000^{O}K), pressures (0.01-10 torr), and silane mixing fractions. A computer program to calculate the equilibrium properties of plasmas containing various ionized species, was obtained from NASA, Lewis Research Center. The program code uses all the species with known thermodynamic functions that are available in its thermodynamic library. For species whose thermodynamic functions are not available, another program (PAC code) can be used to calculate the required functions from spectroscopic constants.

Figure 2-8, illustrates the pressure dependence of calculated equilibrium compositions of Si, Si_2, Si_3, SiH, SiH_2 and SiH_3. At a SiH_4/H_2 ratio of 0.1 and 2000^{O}K silicon containing species rise monotonically with pressure and reach a maximum at 5 torr. Figure 2-9, shows the profiles of silicon containing species for different silane fractions in hydrogen at a temperature of 2000^{O}K and a total pressure of 1 torr. Silicon species reach a maximum in silane mixtures of greater than 30%.

For an optimized high rate deposition, this calculation predicts a system with a silane fraction of 30% in H_2 at a total system pressure of 5 torr, and a system temperature of 2000^{O}K.

Calculations for a phosphorous doped SiH_4/H_2 system as well as for a boron-doped SiH_4/H_2 system, have also been made.

Additional results and further discussion of this work are given in Reference 3.

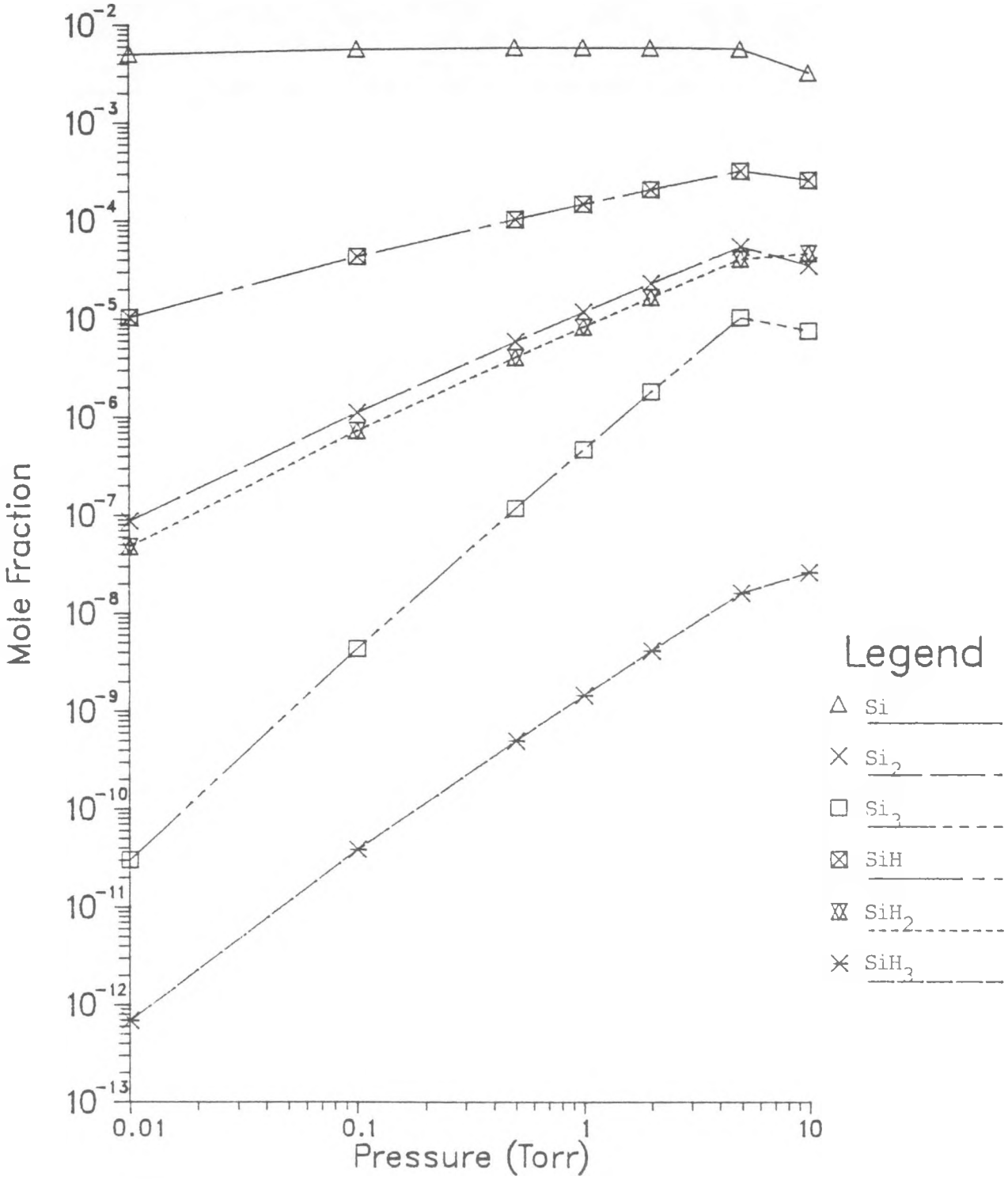

Figure 2-8. Pressure Dependence Of Calculated Equilibrium Compositions Of Si, Si_2, Si_3, SiH, SiH_2, And SiH_3 For SiH_4/H_2 = 0.1 And T = 2000°K

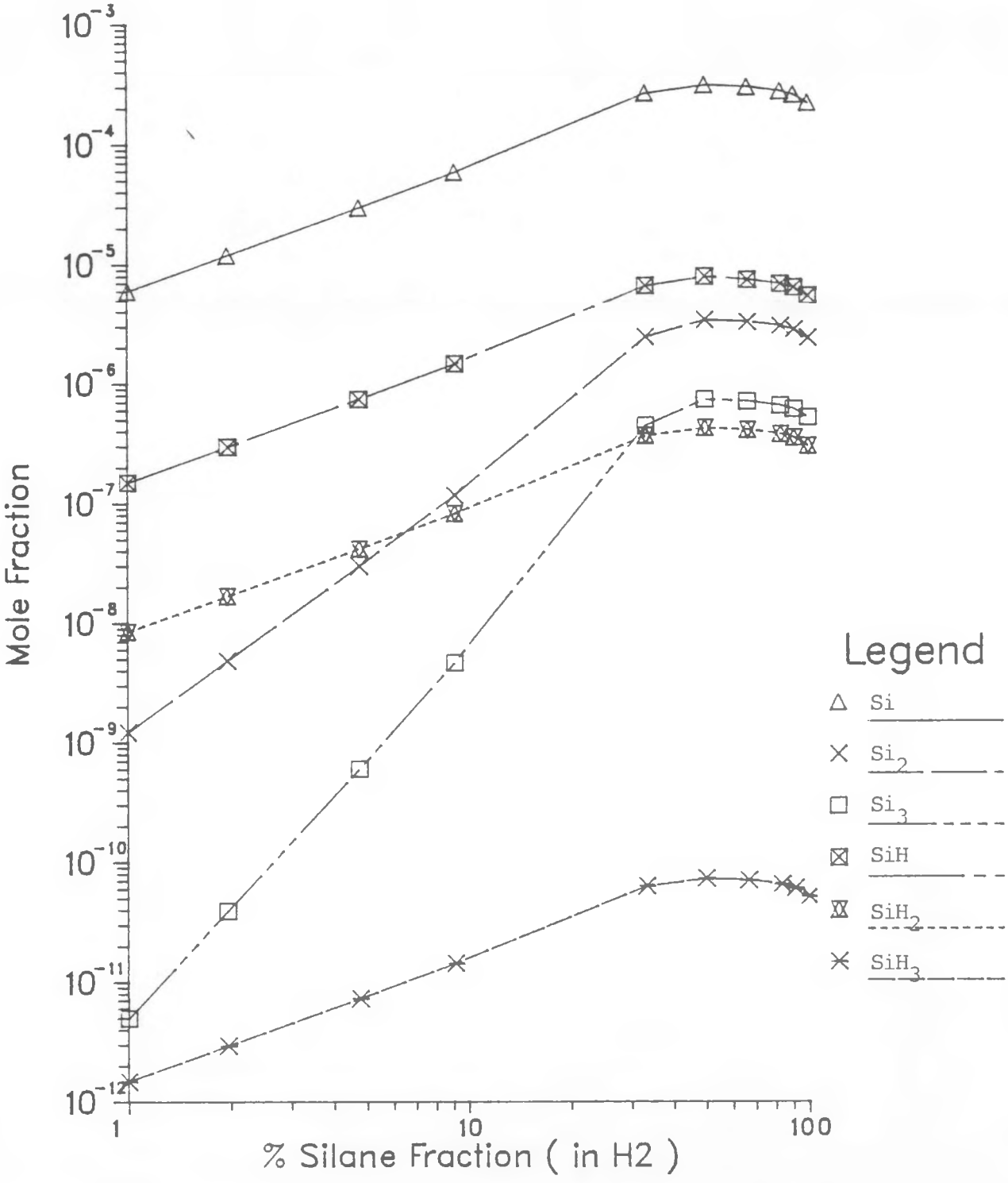

Figure 2-9. Silane Fraction Dependence On Equilibrium Concentrations Of Si, Si_2, Si_3, SiH, SiH_2, And SiH_3 At T = 2000°K And Total Pressure Of 1 Torr

2.2.3.2 Optical Emission Spectroscopy

Optical emission spectroscopy is a valuable diagnostic technique for detecting various species of impurities in a system and for monitoring plasma stability during depositions.

Optical emission spectra were accumulated using a PAR/EG&G optical multi-channel analyzer and the data were stored on a magnetic disk during depositions. Typical emission spectra from a glow discharge of SiH_4/H_2, at a pressure of 1 torr, are shown in Figure 2-10. The species Si^*, H^*, SiH^*, and H_2^* were observed. Likewise, an optical emission spectra from a glow discharge of SiH_4/He, at a pressure of 1 torr, are shown in Figure 2-11. Several peaks of He^* were observed in addition to the species Si^*, H^*, SiH^*, and H_2^*. It was learned that the deposition rate is generally proportional to the SiH^+ intensity. SiH_2^* emission has not been observed, primarily because the emission bands are either weak or fall within the more intense Balmer series for H_2 emission. It was observed that at a given SiH_4 fraction, SiH^*/H^* emission intensity is higher for helium than for hydrogen, as is shown in Figure 2-12.

In addition to optical emission spectroscopy, mass spectroscopy will be used in System One. This will allow us to observe various ionic species in the glow discharge, and will also allow the percentage of silane depletion to be monitored during depositions.

2.2.4 Stability

To minimize the degradation in the conversion efficiency of a-Si solar cells, the light-induced effect was studied in lightly boron-doped a-Si films. Intrinsic films were grown using 0.1 and 1 ppm diborane in the glow discharge gas mixture. An activation energy of 0.85 eV indicates that the Fermi level lies in the mid-gap region. The photocurrent was measured to be 2×10^{-6} A and the ratio of light to dark current was 10^6. The infrared transmission spectrum of the film shown in Figure 2-13 has a bond stretching at 2000 cm^{-1} and a bond rocking at 630 cm^{-1} for the Si-H structural group. The SIMS profile in Figure 2-14 shows an oxygen concentration in the mid 10^{19} range and carbon concentration in the high 10^{19} range for undoped films.

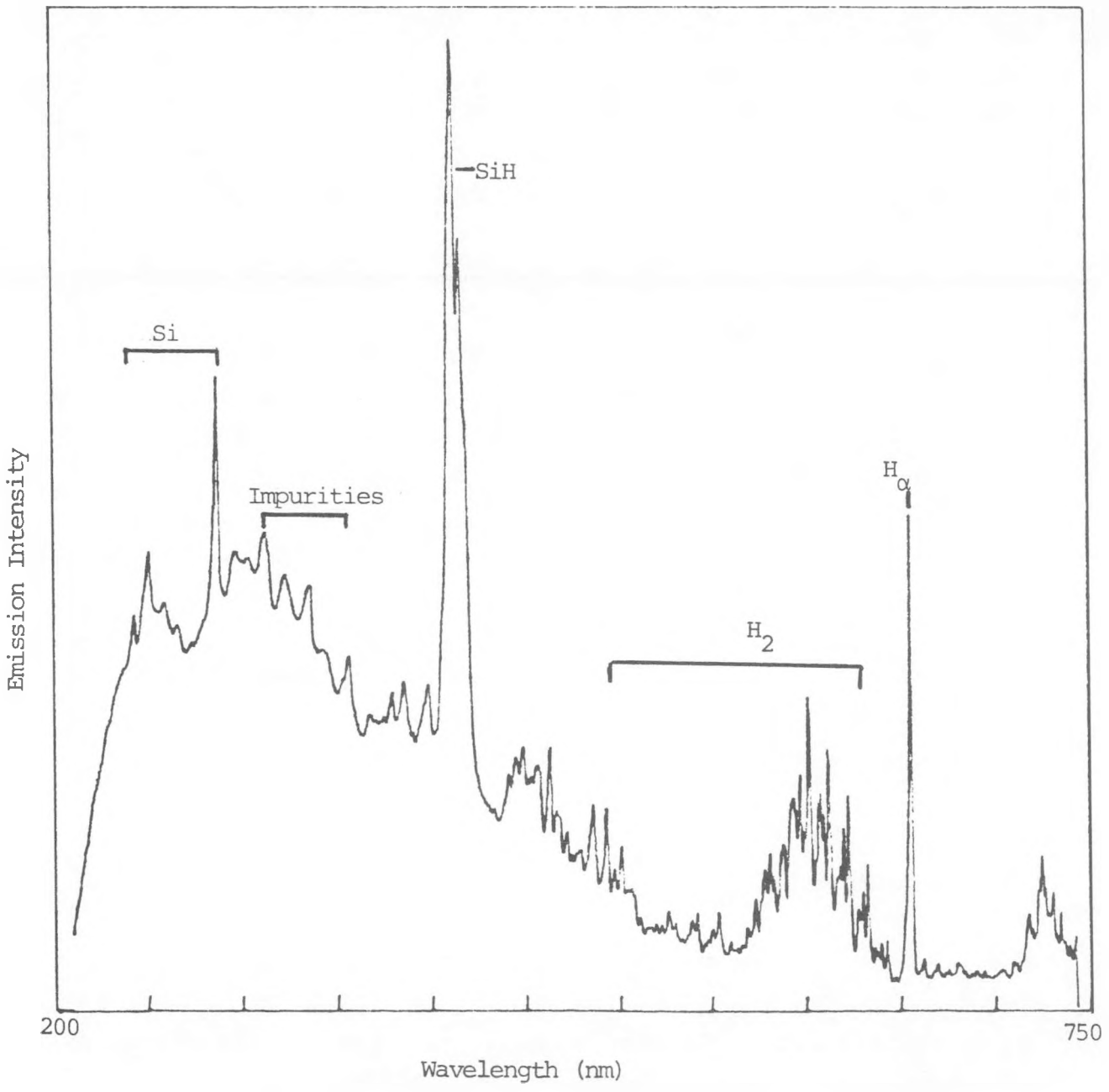

Figure 2-10. Glow Discharge Emission Spectrum Of Silane-Hydrogen Mixture

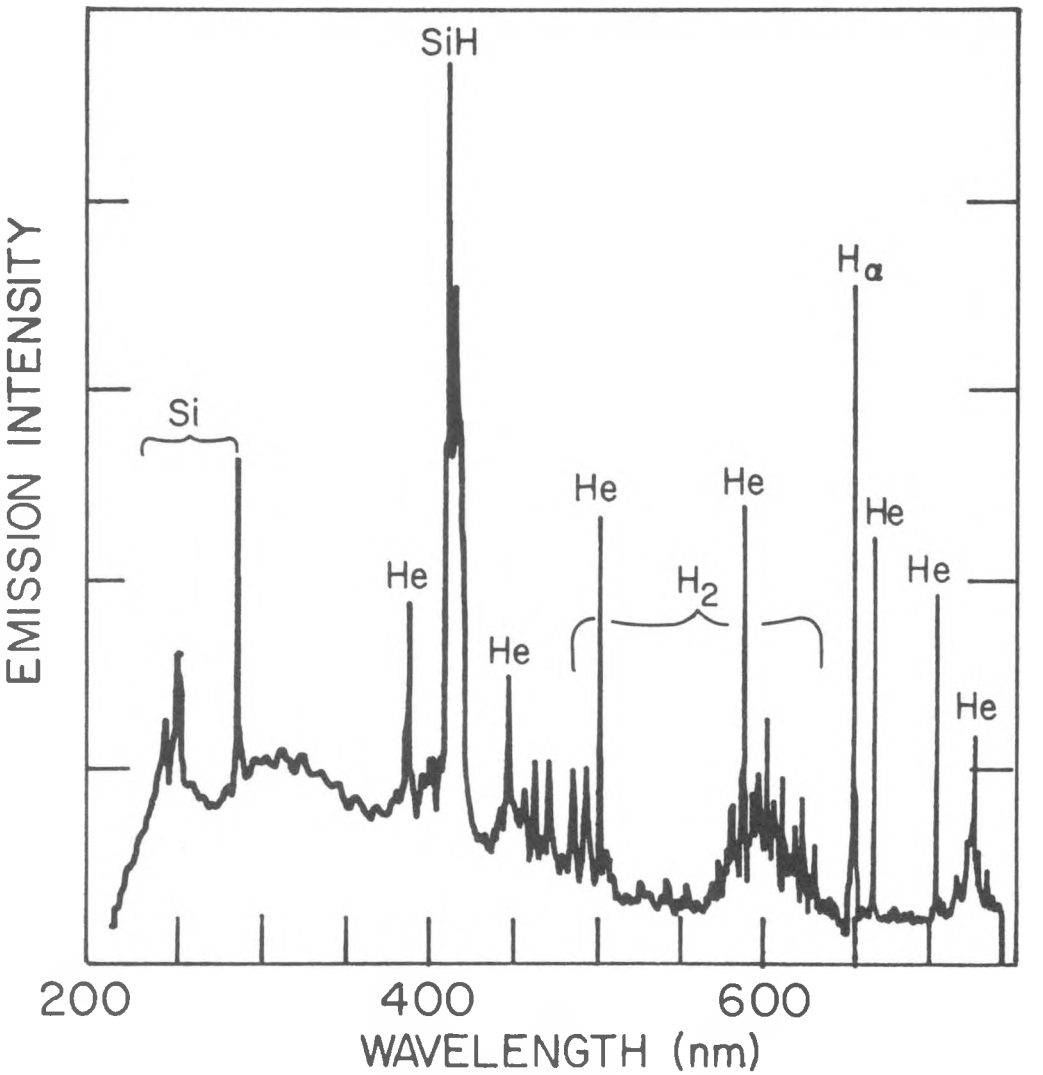

Figure 2-11. Glow Discharge Emission Spectrum Of A Silane-Helium Mixture

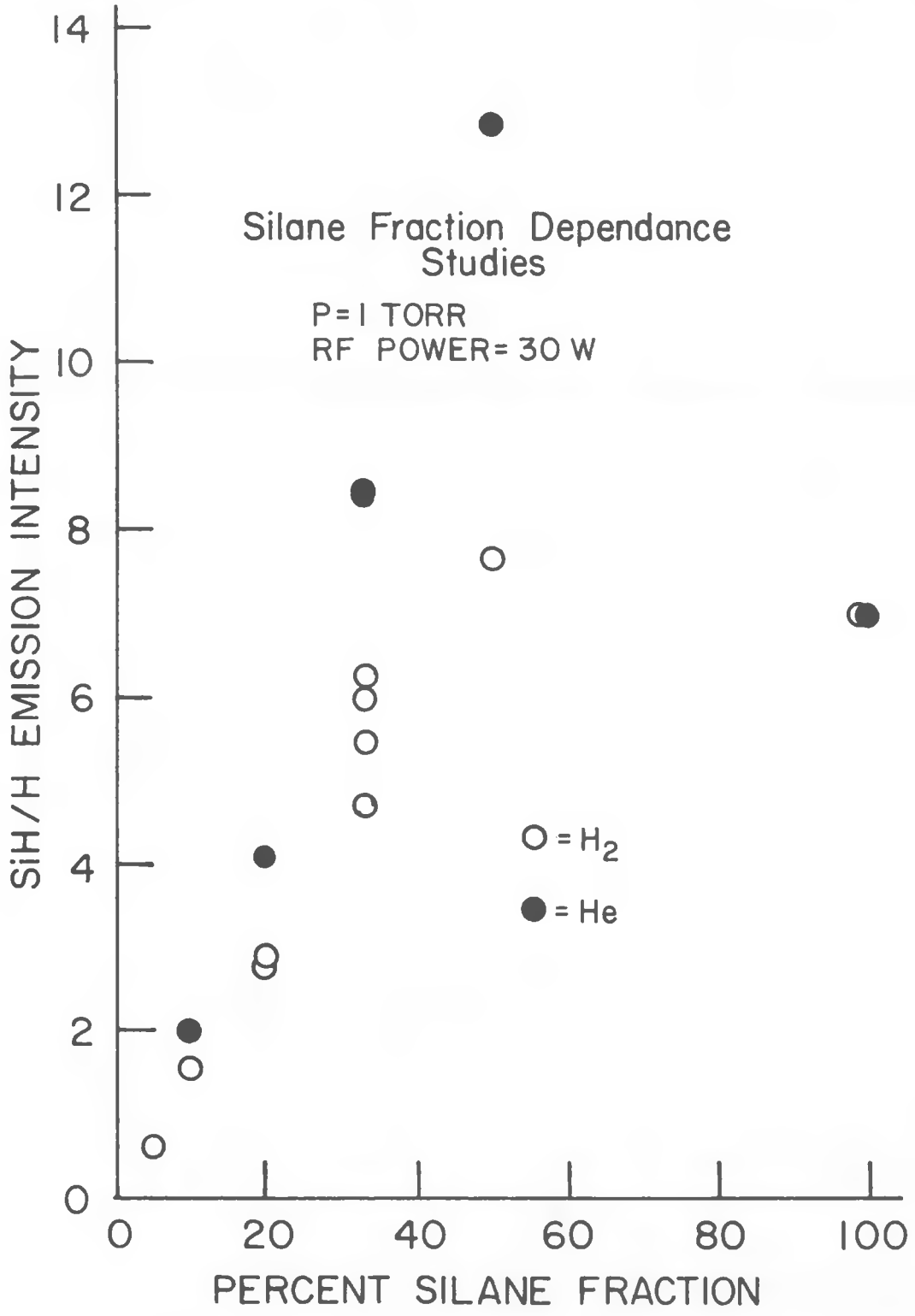

Figure 2-12. Variation Of Deposition Rate As A Function Of the Silane Fraction In H_2 And He

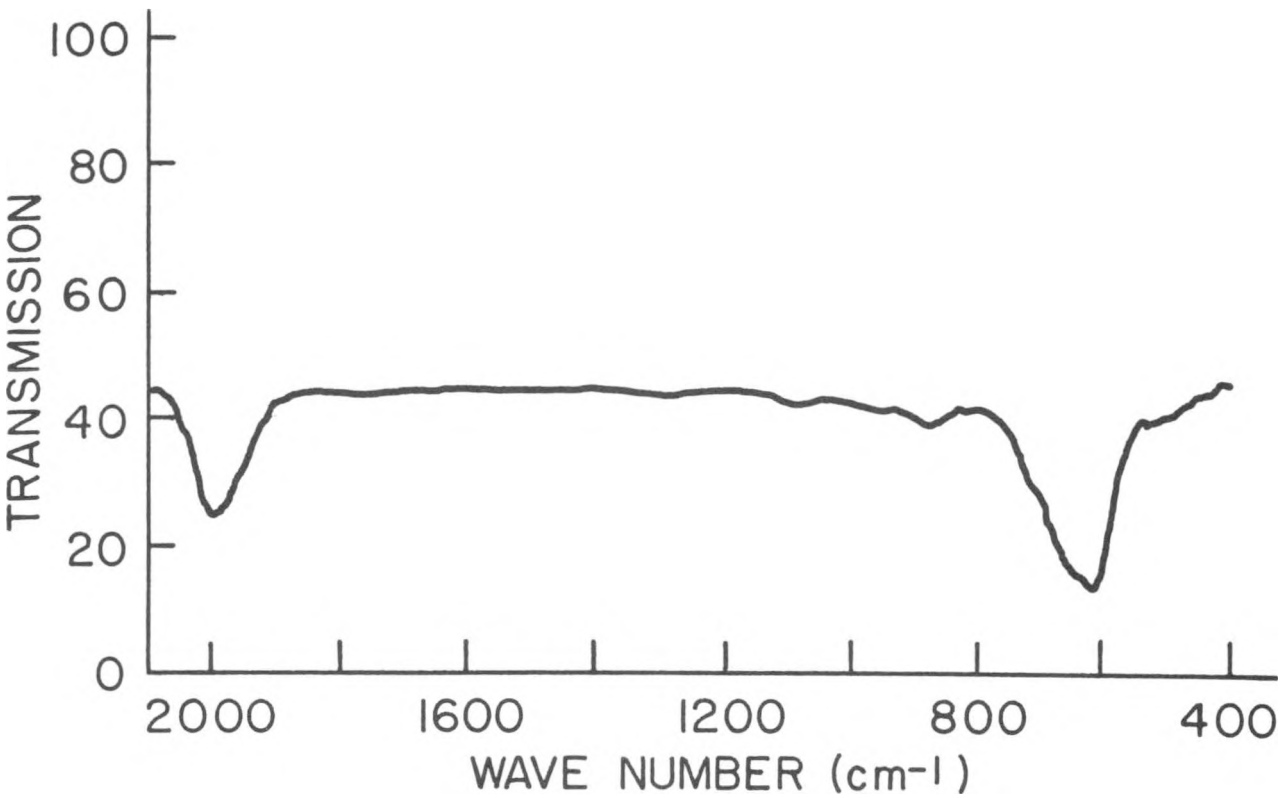

Figure 2-13. Infrared Transmission Spectrum Of Lightly Boron Doped Amorphous Silicon Films

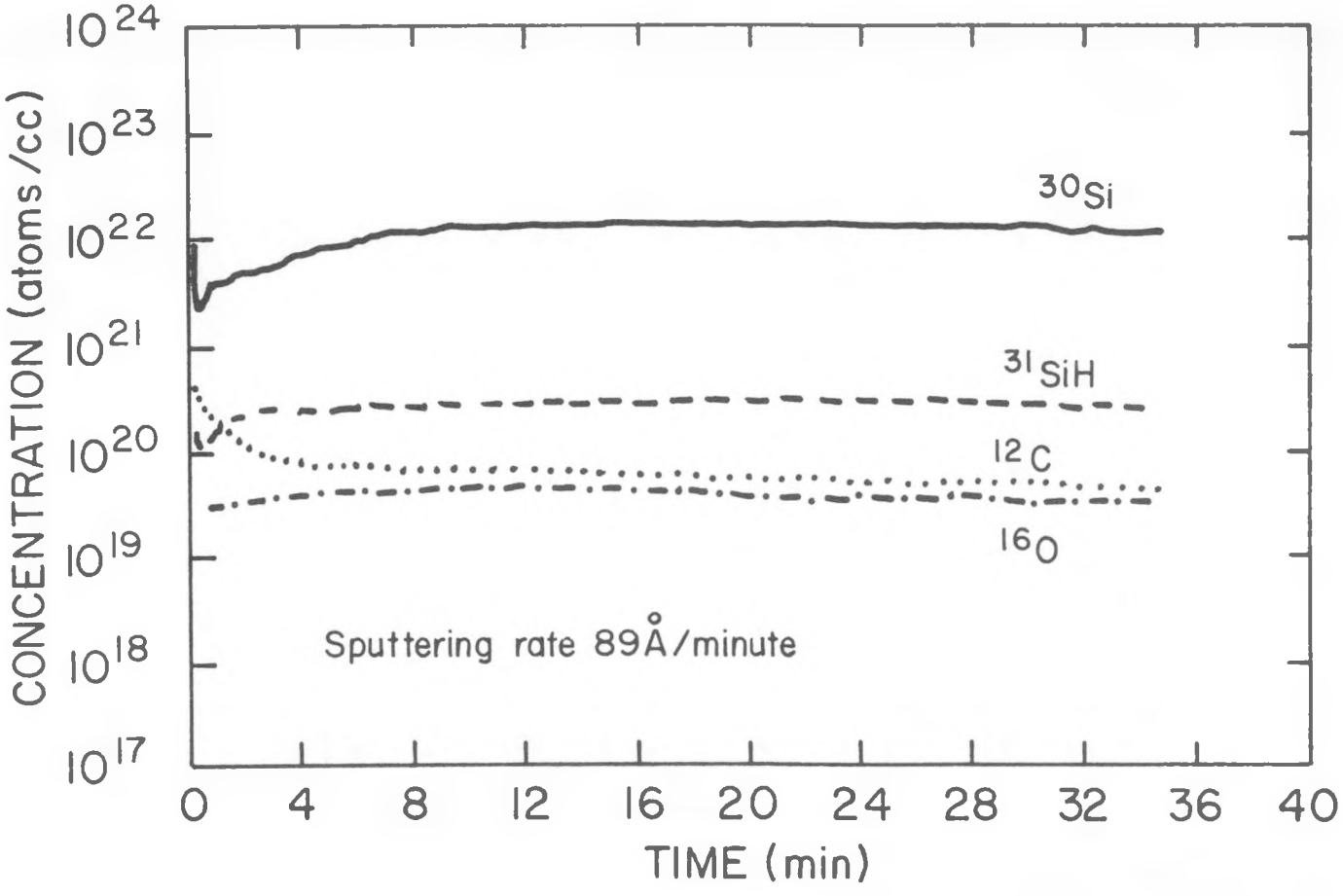

Figure 2-14. A SIMS Profile Of Intrinsic Amorphous Silicon

The boron concentration of lightly boron doped a-Si films is in the low 10^{19} atoms range as illustrated in Figure 2-15. Figure 2-16 illustrates that light boron doping can reduce photocurrent degradation. The photocurrent decreased by 30% after two hours of AM1 illumination and remained stable over the next 70 hours of illumination for an a-Si film grown from a gas mixture having 0.5 ppm diborane. The light current data returned to their original values after three hours of annealing at 160^{o}C.

The mechanism for the light boron doping effect on the stability of amorphous silicon films is not clearly understood. Boron could form B-H bonds thus decreasing the density of Si-H bonds and/or pin the Fermi level to the mid-gap region. Investigations of these phenomena are in progress.

ESR was initiated to study the variation of spin concentration with illumination and with boron dopants. Other dopants such as fluorine, boron and fluorine, and phosphorus compensated with boron were also studied. The Stabler-Wronski effect of the doped films will be studied, using ESR, stress, photoluminescence, SPV, time of flight, and photocurrent measurements. The relationship between the stability and the diffusion of contaminants across the p^{+}/i and i/n^{+} a-Si interfaces will also be studied.

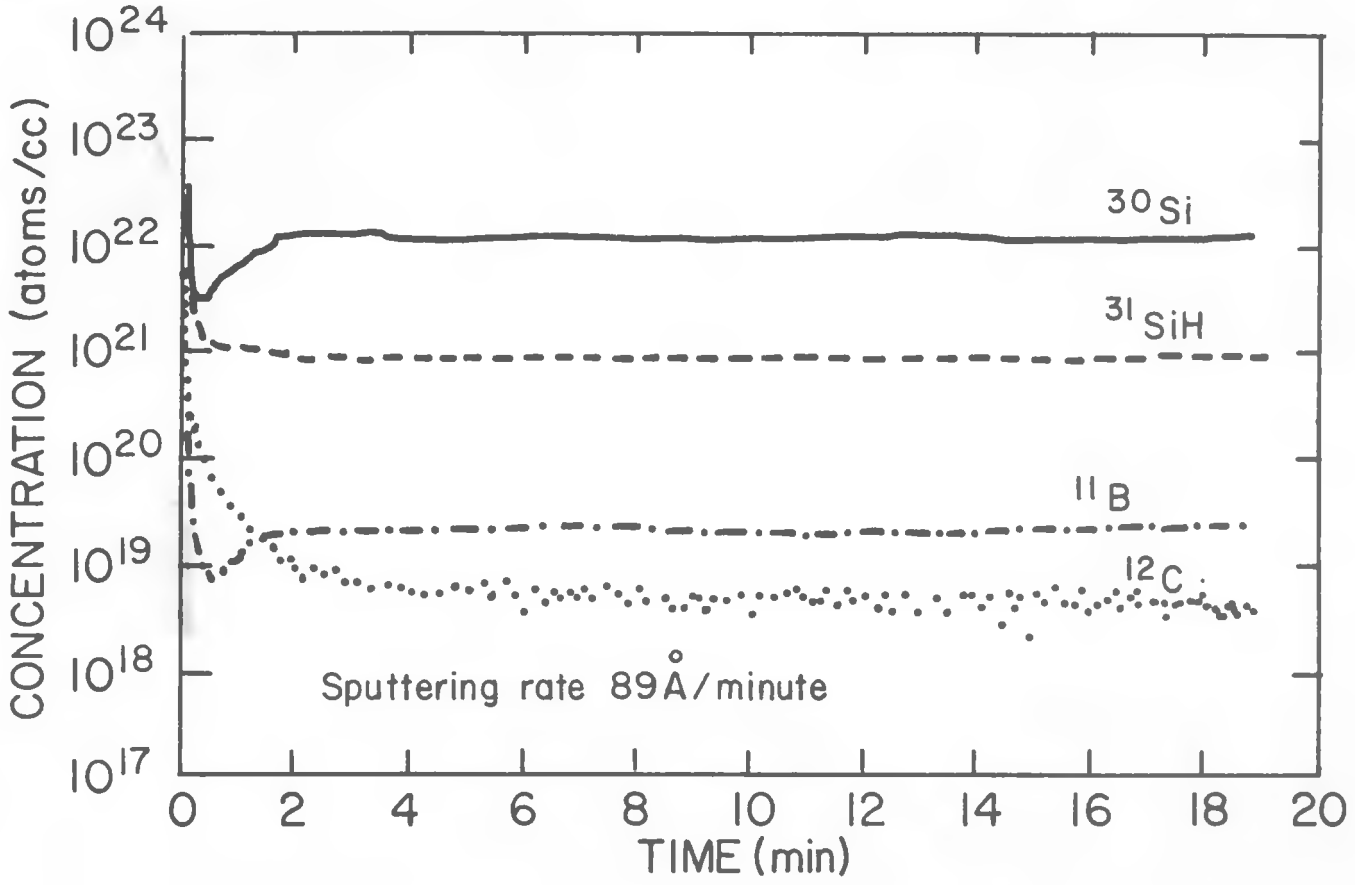

Figure 2-15. SIMS Profile Of Lightly Boron Doped Amorphous Silicon Films

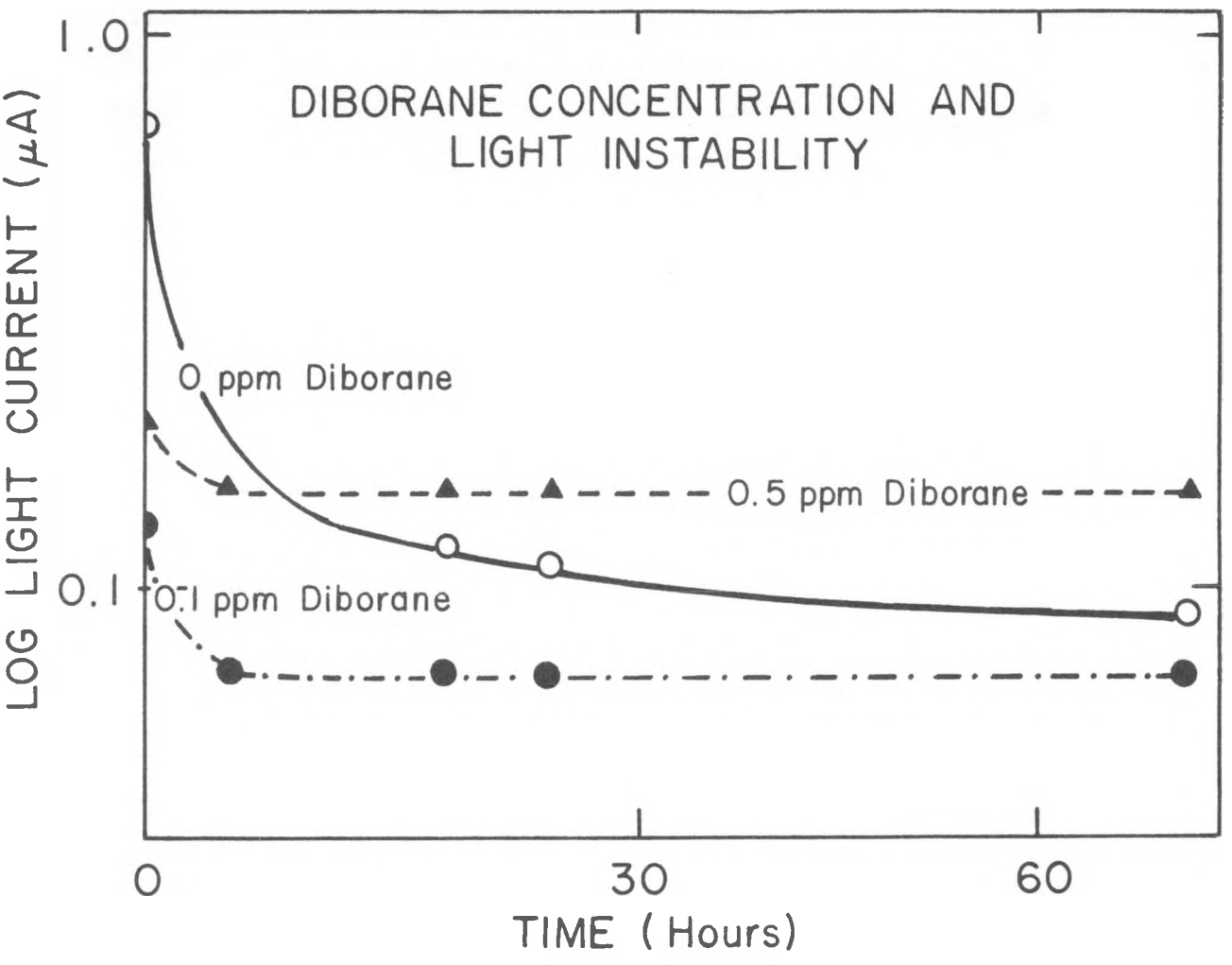

Figure 2-16. Diborane Concentration And Light Instability

3.0 TASK TWO - NON-SEMICONDUCTOR MATERIALS RESEARCH

3.1 Substrate

For a substrate material to be suitable for flexible amorphous silicon solar cell applications, it must be capable of meeting stringent thermal and mechanical demands. Foremost is tolerance to deposition temperatures in excess of 250^{o}C without degradation. A high tensile modulus is also required to prevent the substrate from stretching during deposition. In addition, a moderate coefficient of thermal expansion is necessary in order to limit stress in the a-Si film which results from differential thermal contraction after deposition. The substrate surface must be smooth and free of defects in order to minimize pinhole shorts and shunt occurrences. The substrate need not be transparent but it should be insulating to facilitate a series connected structure.

Most commercially available plastic substrate materials fail to meet the thermal stability requirements. Typical glass transition temperatures T_g, fall far below the 250^{o}C deposition temperature required for a-Si. Furthermore, even decomposition occurs before this temperature is reached. Polyimide is a notable exception. Polyimide meets all requirements mentioned thus far with the possible exception of surface defects. Important thermal and mechanical properties of polyimide films are summarized in Table 3-1 for materials received from four Vendors.*

---

* Vendor Data Sheets

Table 3-1. Typical Thermal And Mechanical Properties Of Polyimide Film

Vendor	A	B	C	D
Tensile Strength (Kg/mm^2)				
at 23^oC	21	20	17	35
at 200^oC	12	15	12	20
Tensile Modulus (Kg/mm^2)				
at 23^oC	350	380	300	700
at 200^oC	180	240	190	390
Coefficient of Thermal Expansion ($10^{-5}/^oC$)	2.1	1.6	1.8	0.6
Heat Shrinkage (% at 250^oC)	.15	.17	.30	.15

The values presented above were confirmed by our measurements. The four vendors' films were further characterized with regard to surface defects and surface roughness. Measurements of total particle count, high corona particles and surface roughness are summarized in Table 3-2. The particle count measurement is accomplished by using a cross-polarization technique which highlights particles that are larger than one micron. High corona particles are those which are larger than ten microns.

Table 3-2. Film Surface Characterization For Various Polyimides

Vendor	A	B	C	C'	D
Total particles ($counts/inch^2$)	38	15	10	15	5
High corona particles ($counts/inch^2$)	1.5	0.8	0	0	0
RMS roughness (nm)	1.9	1.8	6	19	2
Maximum peak-to-valley (nm)	28	13	38	315	20

Vendor C recently introduced the polyimide film labeled C'. It is rougher than the old polyimide, so as to reduce the film-to-film coefficient of friction. This is accomplished by embedding three to five micron spheres (0.1 volume percent) into the polyimide which results in surface protrusions of up to 0.3 microns which are spaced at approximately 30 micron intervals.

3.2 Back Metal Contact

To produce stable, high-efficiency solar cells the back contact must serve three distinct functions. First, it must conduct the photo-generated charge which is collected from the p^+ a-Si layer. In order for resistive losses to be negligible, the sheet resistance should be about 1 ohm/square or less. Second, the back contact must provide a diffusion barrier between the substrate and the a-Si. If impurities are allowed to diffuse through the back contact, they may degrade the active layers of the solar cell. Third, the back contact must have high reflectivity. This is especially important for wavelengths having absorption lengths approximately equal to the a-Si film thickness. It is necessary to maximize the optical absorption within the intrinsic a-Si layer to obtain the best short-circuit current of the cell. The back contact should also exhibit excellent adhesion to the substrate and it should form a suitable electrical contact to the p^+ layer without contaminating the active layers.

For the metal depositions, a Vac-Tec diffusion-pumped roll coater equipped with two 5 x 15 inch cathodes is being used. The system is equipped with a 3 kW RF power supply and a 10 kW dc magnetron power supply. A gas flow controller for three separate gases provides the capability of reactive sputtering. Prior to deposition the polyimide film is out-gassed by passing it through a radiant heater which is mounted in the vacuum system.

3.2.1 Nickel

During this semester Ni has been used as the standard back metal contact and has served as a reliable contact to the p-type amorphous silicon. Ni is not an ideal back metal contact because of its moderately high resistivity (7 micro ohm-cm) and poor reflectivity (40% at 600 nm). One method of increasing the reflectivity is to overcoat the metal with a dielectric such as SnO_2. Sputter deposited Ni films are specularly smooth as shown by the SEM photograph in Figure 3-1. When 600 Å of SnO_2 is sputter deposited on top of the Ni, it too is smooth as shown in Figure 3-2. With this 600 Å film interposed between the Ni and a-Si layer, the reflectivity is increased to 76% at 600 nm.

The current-voltage characteristic of a typical device constructed with Ni as the back electrode and Cr as the front contact is shown in Figure 3-3. Attempts to fabricate devices on Ni/SnO_2 were unsuccessful due to the SnO_2 being reduced to Sn during the glow discharge cleaning step.

3.2.2 Aluminum

Aluminum offers an improvement over nickel as the back metal contact. Its resistivity is 40% of Ni and it reflects 72% at 600 nm, considerably more than nickel's 40%. An additional advantage is that aluminum does not form a specularly smooth surface. Due to its relatively low melting point at 660°C, aluminum can be deposited with a textured surface as shown in Figure 3-4. This textured interface causes diffused scattering of the light which penetrates the a-Si layer. This in turn increases the path length and thus the light absorption within the intrinsic layer, thereby increasing the red response and overall efficiency.

One major drawback for aluminum is that it does not form a suitable contact to p-type a-Si, probably due to diffusion of aluminum into the a-Si. The current-voltage characteristics of a typical Al/pin a-Si/Cr device are shown in Figure 3-5.

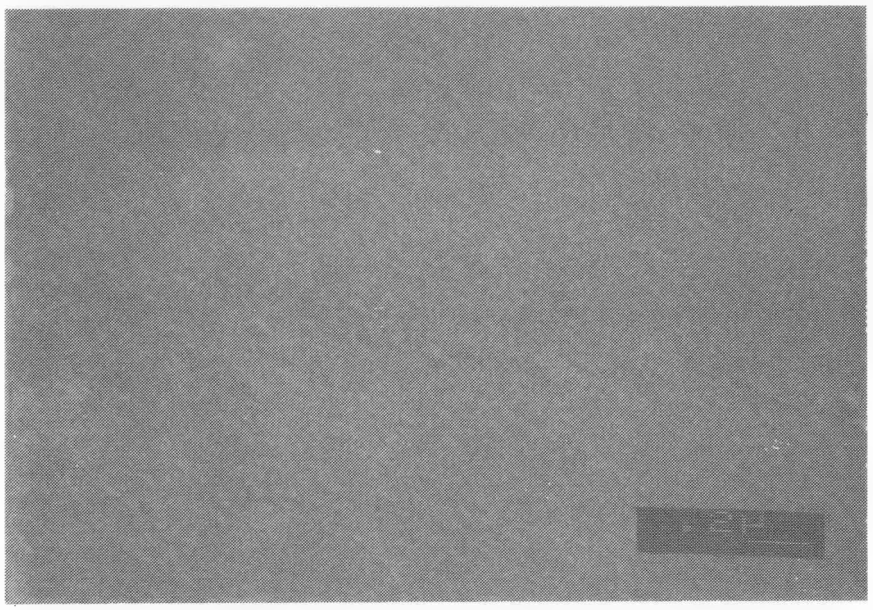

Figure 3-1. SEM Photograph Of 800 Å Ni Polyimide
This 50 KX SEM photo reveals an optically smooth surface.

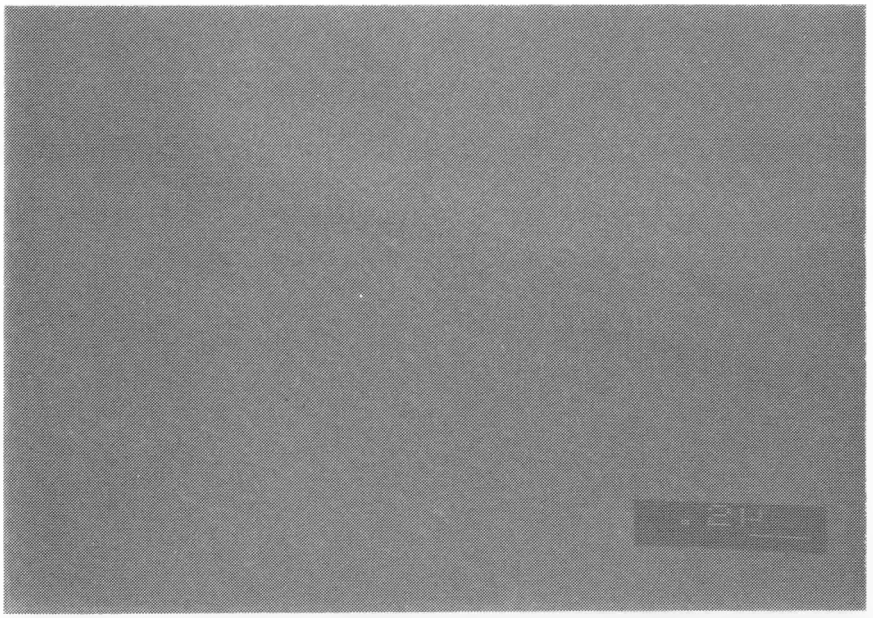

Figure 3-2. SEM Photograph Of 800 Å Ni/600 Å SnO_2
The SnO_2 uniformly covers the Ni film.

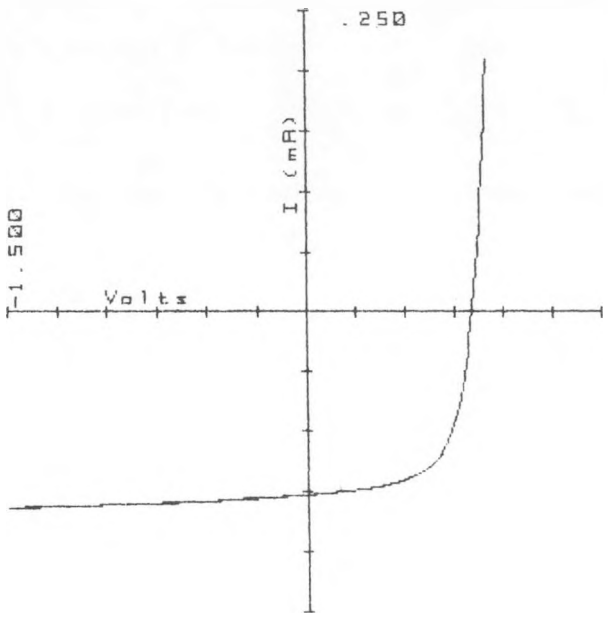

Figure 3-3. Current-Voltage Characteristic Of Typical Ni/pin/Cr Device
The open current voltage is 0.84 V and the fill factor is 62%.

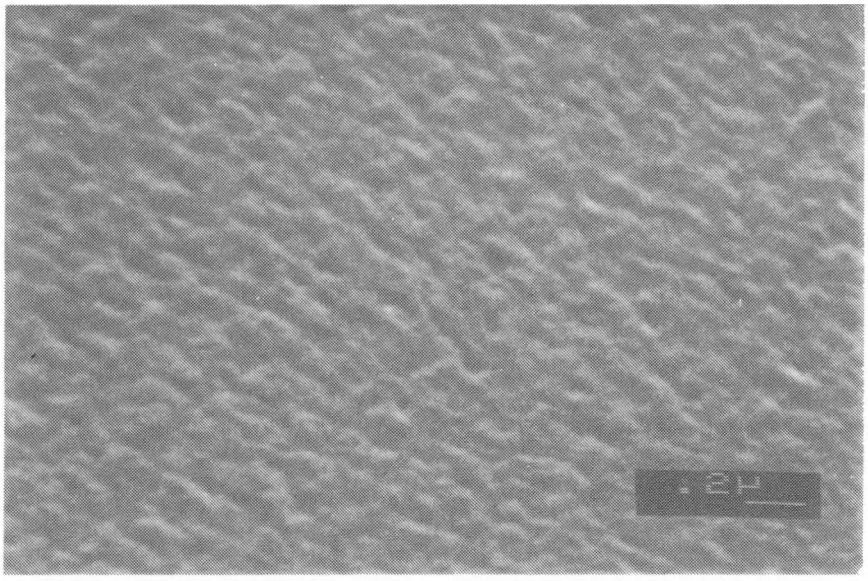

Figure 3-4. SEM Photograph Of 800 Å Of Aluminum On Polyimide
Note the textured surface.

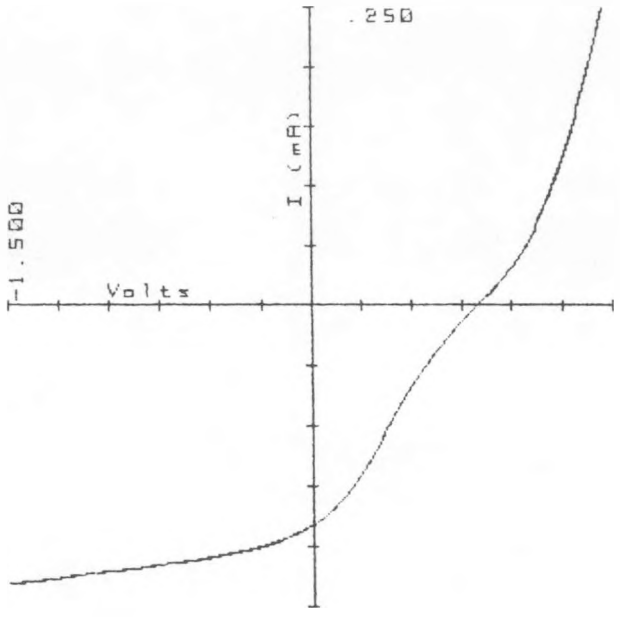

Figure 3-5. Current-Voltage Characteristics Of A Representative Al/pin a-Si/Cr Device On Polyimide
Note evidence of a contact problem in the vicinity of V_{oc}.

3.2.3 Aluminum/Tin Oxide

In an attempt to solve the Al diffusion problem as well as enhance the reflection from the back contact, 600 Å of SnO_2 was sputter deposited onto the aluminum film. The reflectivity is increased from 72% to about 90% for 600 nm light by introducing the SnO_2 film. The SnO_2 again conforms to the metal as shown in Figure 3-6, thus preserving the texture of the aluminum.

The current-voltage characteristics of devices made on SnO_2 show that this is not a good contact to p^+ a-Si. These devices fell into three categories. The best devices suffered from a low fill factor ($\leq$ 0.50) as shown in Figure 3-7(a). The second group not only exhibited a low fill factor but also a large shunt as shown in Figure 3-7(b). The rest of the devices were either unstable or completely shorted.

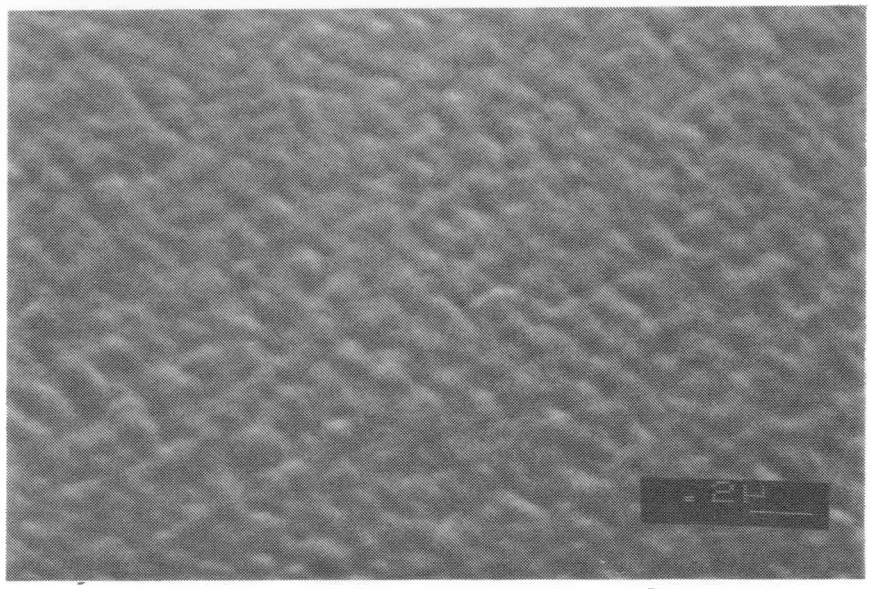

Figure 3-6. SEM Photograph Of 800 Å Al/600 Å SnO_2 On Polyimide
Note that the texture is similar to that of aluminum alone as shown in Figure 3-4.

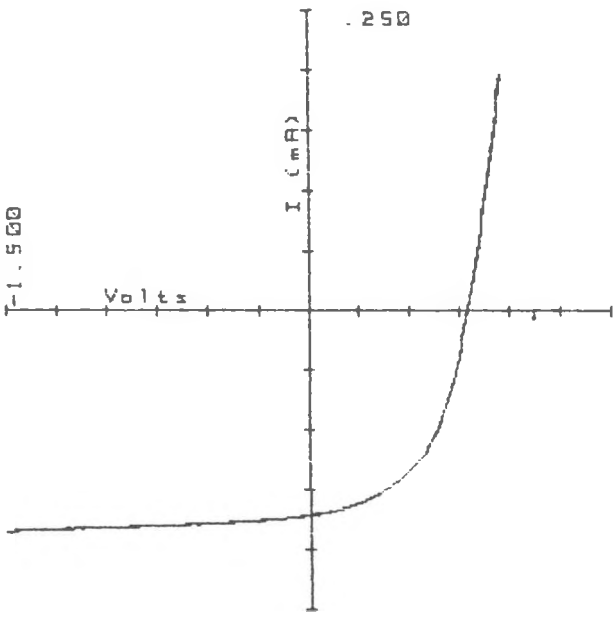

(a)

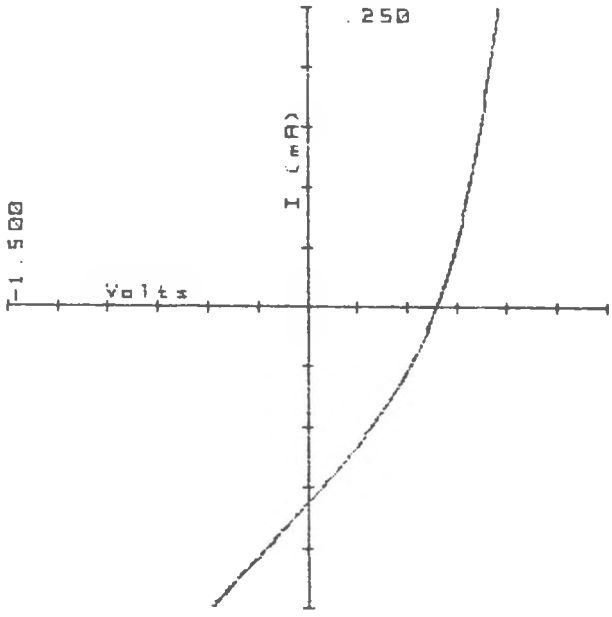

(b)

Figure 3-7. Current-Voltage Characteristics For Representative Al/SnO_2/Cr Devices On Polyimide
Note the low fill factor and large shunt current.

3.2.4 Aluminum/Stainless Steel

The aluminum/stainless steel bilayer has been shown by Teijin to be an effective electrode for a-Si photovoltaic devices [4]. Stainless steel layers as thin as 25 Å were effective in preventing Al contamination of the a-Si but overall reflectance is reduced. For a 50 Å thick layer of stainless steel, the light absorbed by the back contact is increased by approximately 50%. However, the advantages of high conductivity and textured surface are maintained. A series of Al/stainless steel/pin a-Si/Cr devices were constructed in which the stainless steel layer thickness was the only parameter varied. It was demonstrated that for stainless steel thicknesses of 25 Å, 50 Å, 100 Å, and 200 Å, devices were obtainable having fill factors in excess of 60%. The current-voltage characteristics for a typical device incorporating a 25 Å stainless steel barrier are shown in Figure 3-8.

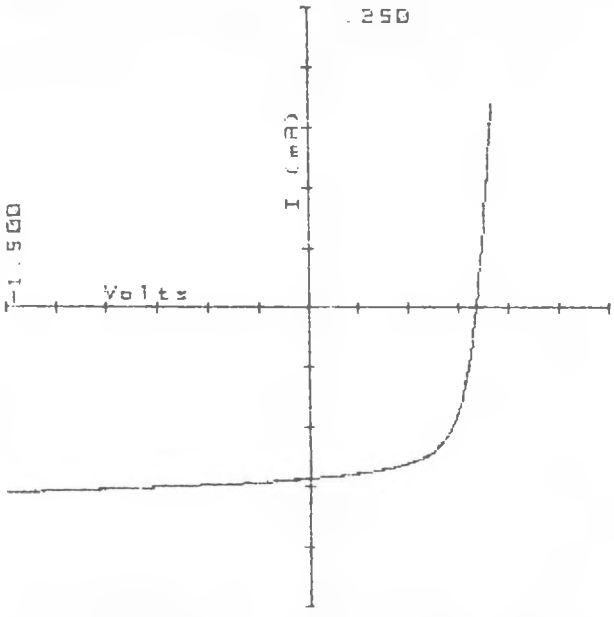

Figure 3-8. Current-Voltage Characteristics For A Representative Al/Stainless Steel/pin a-Si/Cr Device
The Al and stainless steel thicknesses were about 700 Å and 25 Å respectively. The Fill Factor for this device was 0.63.

These studies have demonstrated that aluminum can be used for the back metal contact provided that a diffusion barrier is used. Additional work is under way to test materials other than SnO_2 for this purpose.

3.3 Transparent Front Contact

The low optical absorption and the high electrical conductivity requirements of the front contact are accomplished most successfully by using indium-tin oxide (ITO). In the past, a major drawback in using ITO has been its tendency to yield free In to the a-Si, thus causing degradation in cell efficiency. We believe this problem can be minimized by making use of a low-temperature sputter deposition technique for the ITO exclusively. This is the approach we have pursued.

3.3.1 ITO Depositions

3.3.1.1 Batch Coater

We are using a batch coater to facilitate efficient and timely progress in small area device testing and interface studies. The batch coater is equipped with a shuttered 5" x 15" target driven by a 1 kW RF power supply. The samples to be coated are covered with a polyimide mask and clamped to a heater block which is mounted on a water-cooled table. The ITO films are deposited by reactive sputtering from an In/Sn target. The deposition rates are kept very slow (approximately 10 Å/minute) in order to prevent damage due to excessive heating and high RF fields. Some films are deposited through a grounded copper screen mesh for the same purpose. Film thicknesses of 700 Å and less than 100 ohms/square sheet resistance have been obtained on a routine basis with this system. Transmission of films deposited on glass is excellent (greater than 80% for wavelengths above 450 nm). The films are smooth and featureless as shown in Figure 3-9. When deposited on amorphous silicon, the ITO conforms to the texture of the amorphous silicon film as shown by Figure 3-10. ESCA analysis of these films indicates atomic composition of 63% oxygen, 33% indium and 3.7% tin. These ITO films are very stable under ambient conditions.

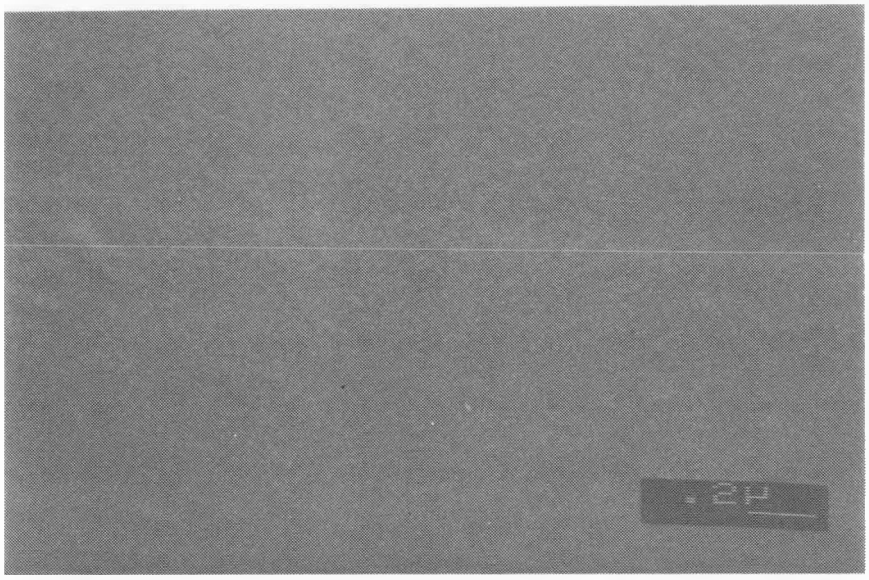

Figure 3-9. 50 KX SEM Of ITO From Batch Coater On Glass
This 700 Å thick film is smooth and featureless.

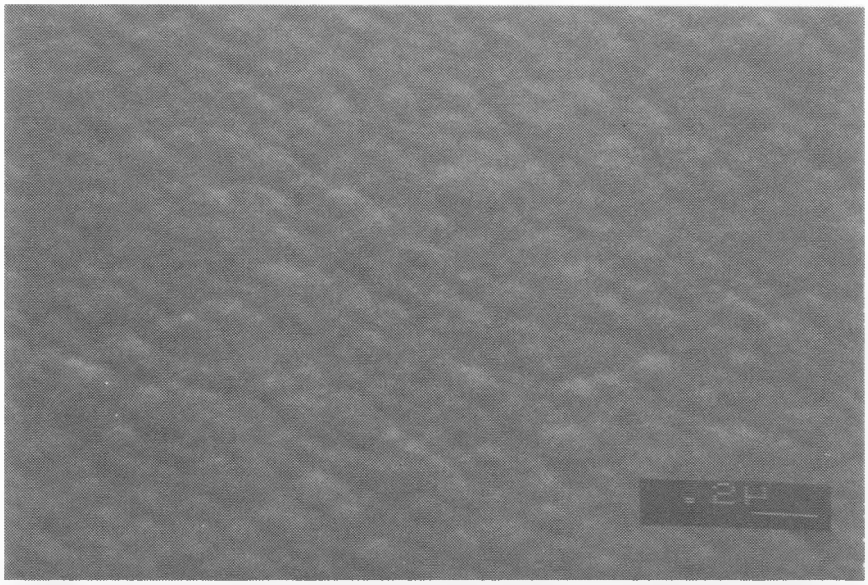

Figure 3-10. 50 KX SEM Of Device Using ITO From Batch Coater
The ITO replicates the texture of the amorphous silicon film.

3.3.1.2 Continuous Coater

A process for sputter depositing high quality ITO films at low temperatures in a roll-to-roll deposition system is being developed. This sputtering system is capable of depositing ITO layers on 4-inch wide rolls. Currently, 2100 Å thick films deposited in this system have a sheet resistance of approximately 35 ohms/square. Initially, devices made in this system suffered from unstable ITO. The sheet resistance of the ITO increased rapidly in room air. Elemental analysis by ESCA revealed the composition of these films to be 54% oxygen, 32% indium, 1.8% tin and 10% carbon. The instability is presumed to be due to the large carbon content. The source of the carbon was traced to the method of splicing the samples together and possible over-heating of the film edges. Measures were taken to minimize those problems and stability of current films is greatly improved.

These films are highly transparent as shown by the spectra in Figure 3-11, for one such film deposited on polyester.

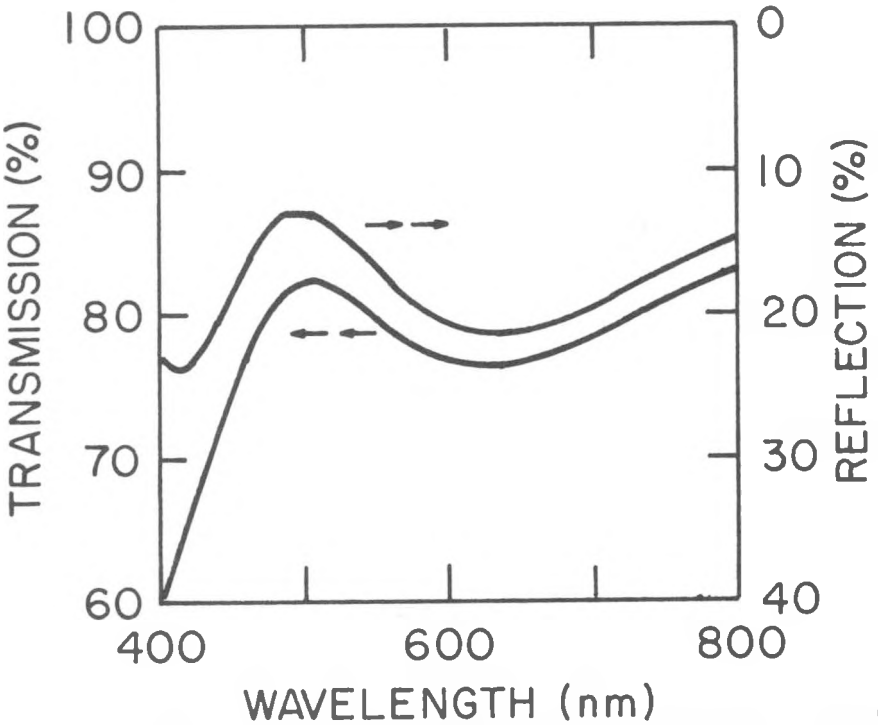

Figure 3-11. Transmission And Reflection Spectra For 2100 Å ITO Film Produced In Continuous Coater
Note the absorption loss is 2-5% over the useful spectral range.

A significant difference exists between the texture of these films and those produced in the batch coater. As shown in Figure 3-12, the ITO films produced in the roll coater exhibit a fine texture with domains of about 200 Å in diameter. The coarser texture seen in this SEM of 0.2 - 0.3 microns is that of the amorphous silicon.

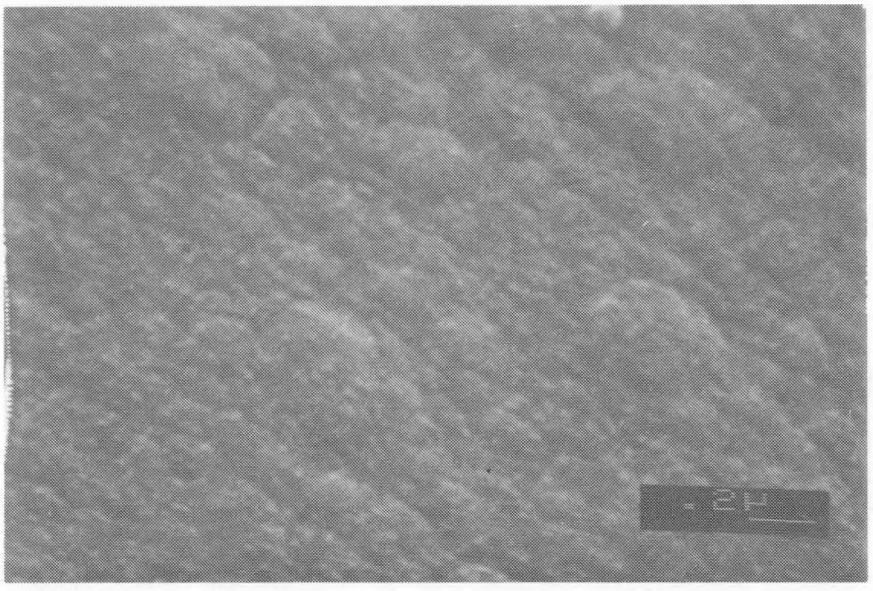

Figure 3-12. 50 KX SEM Of Device Using ITO From The Continuous Coater Notice the fine texture of 200 Å diameter domains.

3.3.2 ITO/Amorphous Silicon Interface

The most sensitive property of the ITO/a-Si interface are the current-voltage characteristics of a device which incorporates this interface. In order to obtain useful information, however, one must establish what the contributions to the I-V characteristics are from other interfaces and from the materials. This is particularly true when heat treating or aging is involved since each interface and material could undergo a change.

In order to study the ITO/a-Si interface we chose to heat-treat devices at 130^{o}C and compare device characteristics before and after heat-treating. The choice of 130^{o}C is not completely arbitrary. The temperature should be significantly above expected operating temperatures in order to be meaningful. On the other hand the temperature should not be so high as to introduce deterioration mechanisms that will be negligible at operating temperature. We were able to establish that the other interfaces and materials involved were not affected by the heat treatment. Control devices were constructed adjacent to the test device using semi-transparent Cr contacts in place of the ITO. No significant change occurred in the devices with the Cr contact subsequent to heat treatment. The devices with ITO contacts deteriorated as shown in Table 3-3.

Table 3-3. Device Characteristics Of Heat-Treated Ni/pin a-Si/ITO Devices. The devices were held at 130^{o}C for intervals of 1, 2 and 16 hours.

Cumulative time (hours)	0	1	3	19
Fill Factor (%)	42.2	40.7	29.5	22.2
Open Circuit Voltage (Volts)	0.82	0.84	0.84	0.84
Short Circuit Current (mA/cm^2)	8.49	8.52	7.97	4.11

4.0 TASK THREE - SOLAR CELL RESEARCH

4.1 Defect Characterization In Amorphous Silicon Solar Cells

A primary concern in fabricating a-Si solar cells on polyimide substrate involves the possibility that the higher defect density of the polyimide, as compared to glass, will cause unacceptable shunting in large area cells. Figure 4-1 shows a micrograph of polyimide substrate. The defect density of polyimide is much higher than that of glass substrates. When proper substrate cleaning techniques are incorporated into the device fabrication process, the higher defect density of polyimide does not affect device quality.

A type 35C JEOL scanning electron microscope with a type 103B G&W current amplifier in electron beam induced current (EBIC) mode is being ued to investigate the relationship between substrate and fabrication induced defects, and charge collection efficiency in our solar cells.

In Figure 4-2, an EBIC image of a low resistivity shunt is shown. The bright areas represent the sites where all the generated current is being collected by the contacts. The shunt path is located in the middle of the dark area. The gray area radiating outward from the shunt indicates that a portion of the current is being collected and the remainder is being directed through the shunt path. The SEM image of this area shows no indication of substrate surface damage that accounts for the shunt.

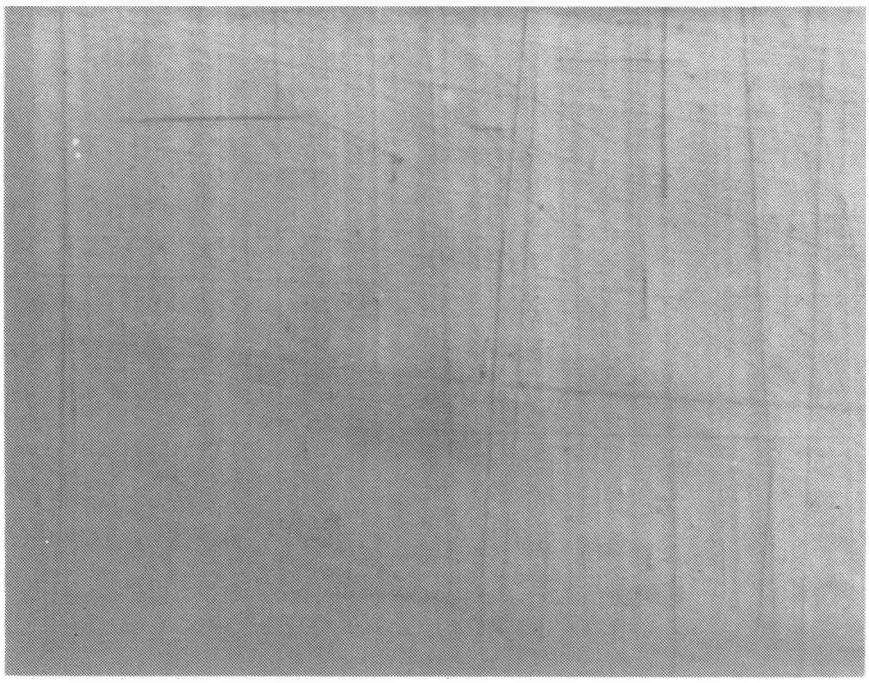

Figure 4-1. 75X Micrograph Of Polyimide Showing Line And Point Defects

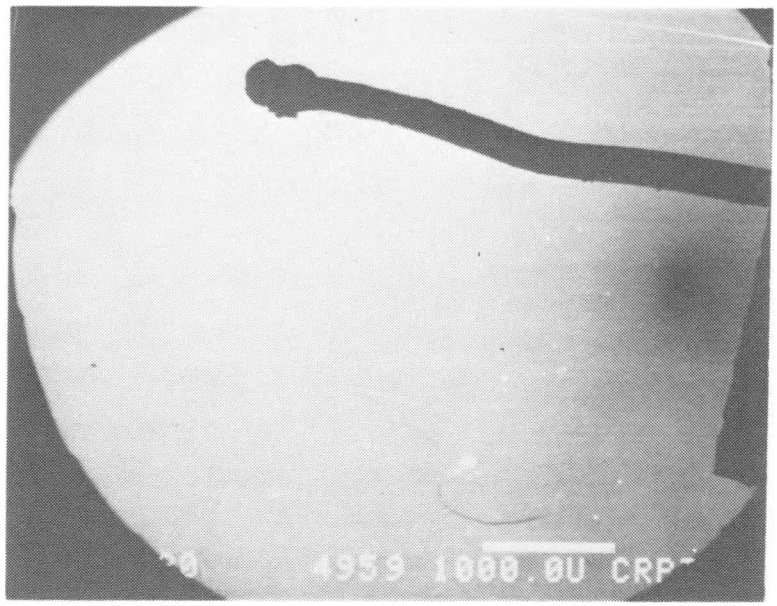

Figure 4-2. EBIC Image Of A PV Device Showing Classic Shunt Area

Four different defect modes have been identified: 1) open or masking type defects, 2) shunts caused by dust particles on the substrate prior to deposition, 3) defects caused by inclusion of silicon dust into the device during deposition, and 4) surface damage.

In Figure 4-3 the EBIC scan shows a distinct, dark area (no current collection) which is surrounded by a light area. In this type of open or masking defect, no current is drawn from the surrounding area. X-ray back scattering indicates that since there was a metal top coat in the affected area, the defect was caused by a non-contact condition on the bottom of the cell.

Figures 4-4a and 4-4b show an EBIC image and a high magnification SEM image of a classic shunt. It appears that a loose dust particle on the substrate surface caused a hollow area to form around its outer edges during deposition. This type of defect is the most detrimental to producing reliable large area devices. In this particular example, the open circuit voltage was reduced by 50% on a 0.3 cm^2 sample.

Another type of shunt defect results from the inclusion of silicon dust into the active layers during device fabrication. This can occur when deposition conditions are not optimized and/or an improper reactor gas flow pattern is used. Under these conditions, large amounts of silicon dust are generated and incorporated into the devices. See Figure 4-5. Defects of this type are also of the masking or open variety and do not appear to have a detrimental effect on device characteristics unless a large number are present, causing the active area to be reduced significantly.

The last type of defect is caused by surface damage as shown in Figure 4-6. This defect results from either insufficient top contact or the presence of particulate contamination in the top layer. Masking defects of this type do not affect the open circuit voltage of the device, however, current output is reduced because of the decrease in active area.

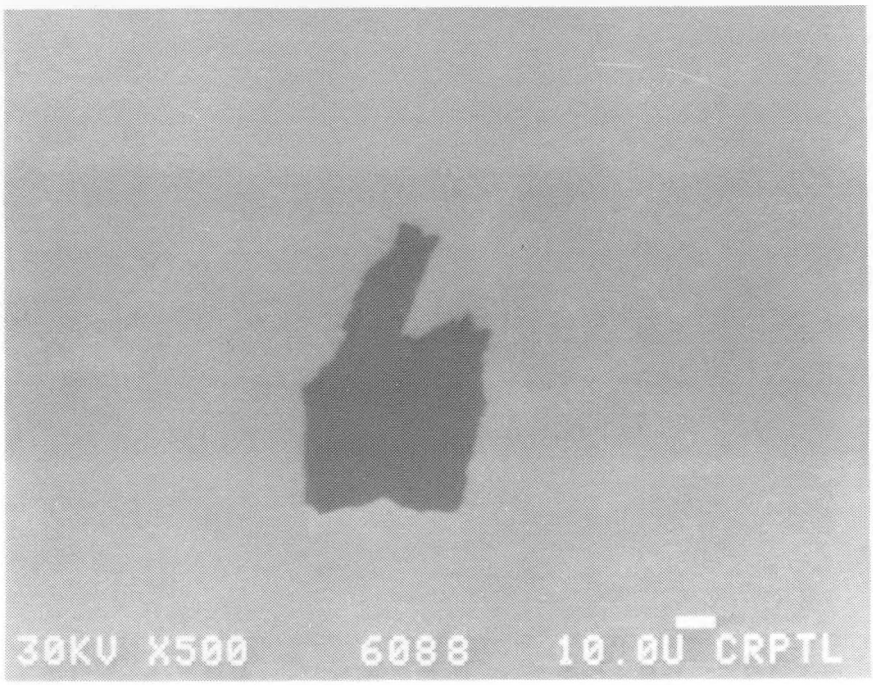

Figure 4-3. EBIC Image - Missing Contact On The Bottom Of The Cell

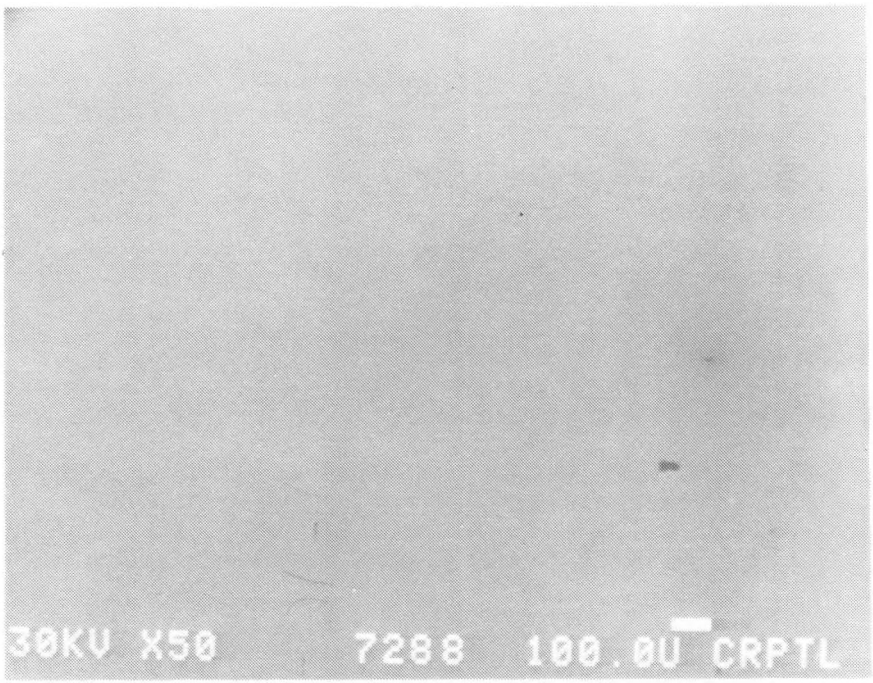

Figure 4-4 (a) EBIC Image Of A Classic Shunt Area On A PV Device

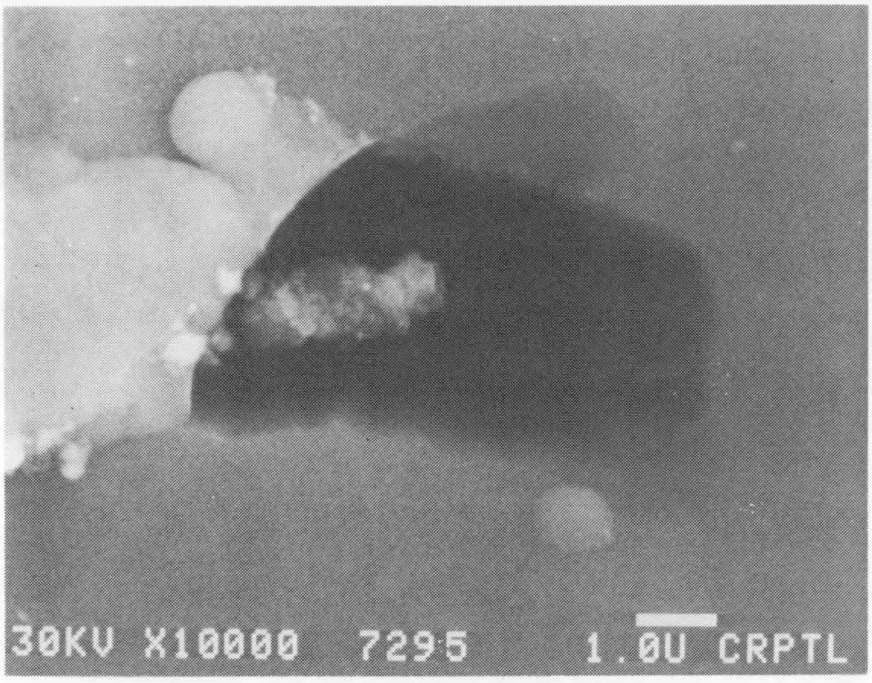

Figure 4-4 (b) 10,000X Magnification SEM Image Of Shunt Area Shown In 4-4 (a)

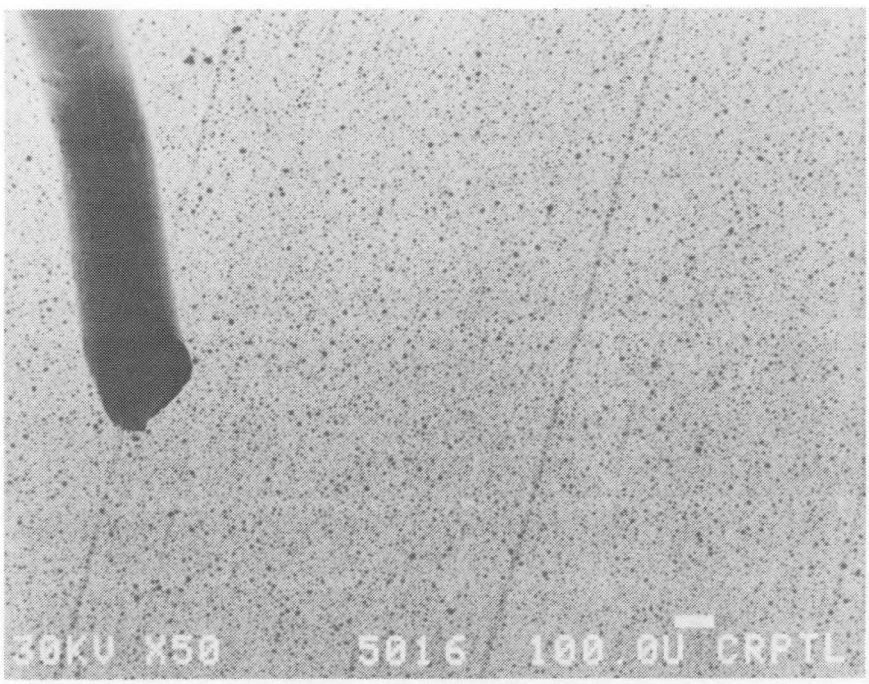

Figure 4-5. EBIC Image Of A PV Device Showing The Inclusion Of Silicon Dust Particles

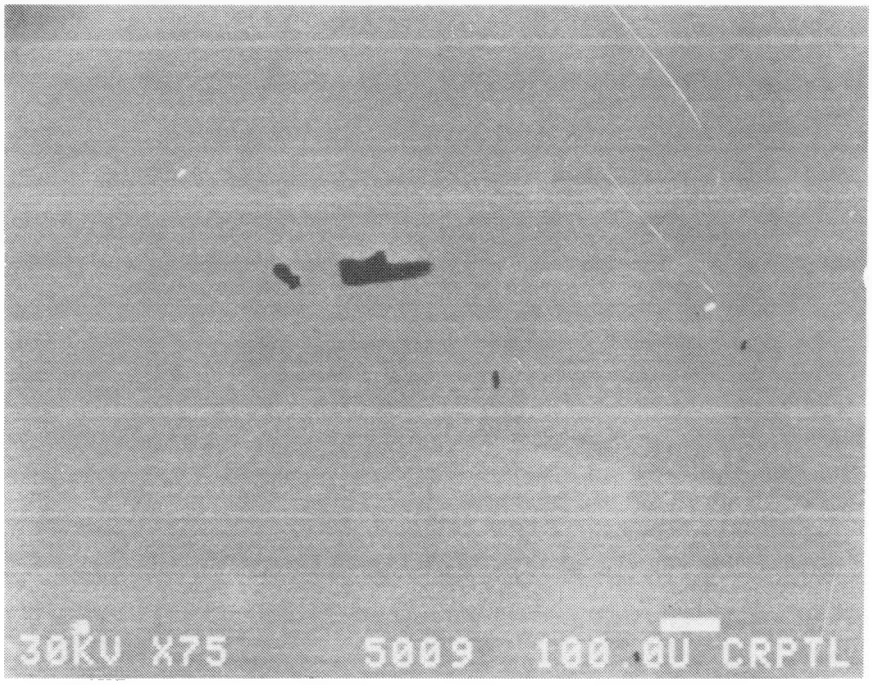

Figure 4-6. EBIC Image Of A PV Device Showing The Effect Of Surface Damage

From the above observations it has been determined that substrate surface cleanliness is the most important criteria relative to producing reliable a-Si devices. Shunt defects can result from dust on the substrate surface, as well as from loose particles of metal generated either during the deposition of the bottom metallized layer, or in the metal scribing step.

To determine the effect that substrate cleaning has on device yield, a study was performed in which Schottky barrier devices were fabricated on substrates which had been cleaned using various methods. In one technique, a 3M brand "Masterwipe" mechanical cleaner was used with ionized nitrogen. This cleaner consists of an upper and lower roll of soft nonwoven fabric through which the substrate is passed, followed by an antistatic device which neutralizes static charge with ionized air produced by alpha particles from a Polonium 210 source. The substrate surface was sprayed clean with ionized nitrogen and then subjected to an additional cleaning step a varying number of times. Schottky devices were fabricated and the results are shown in Figure 4-7.

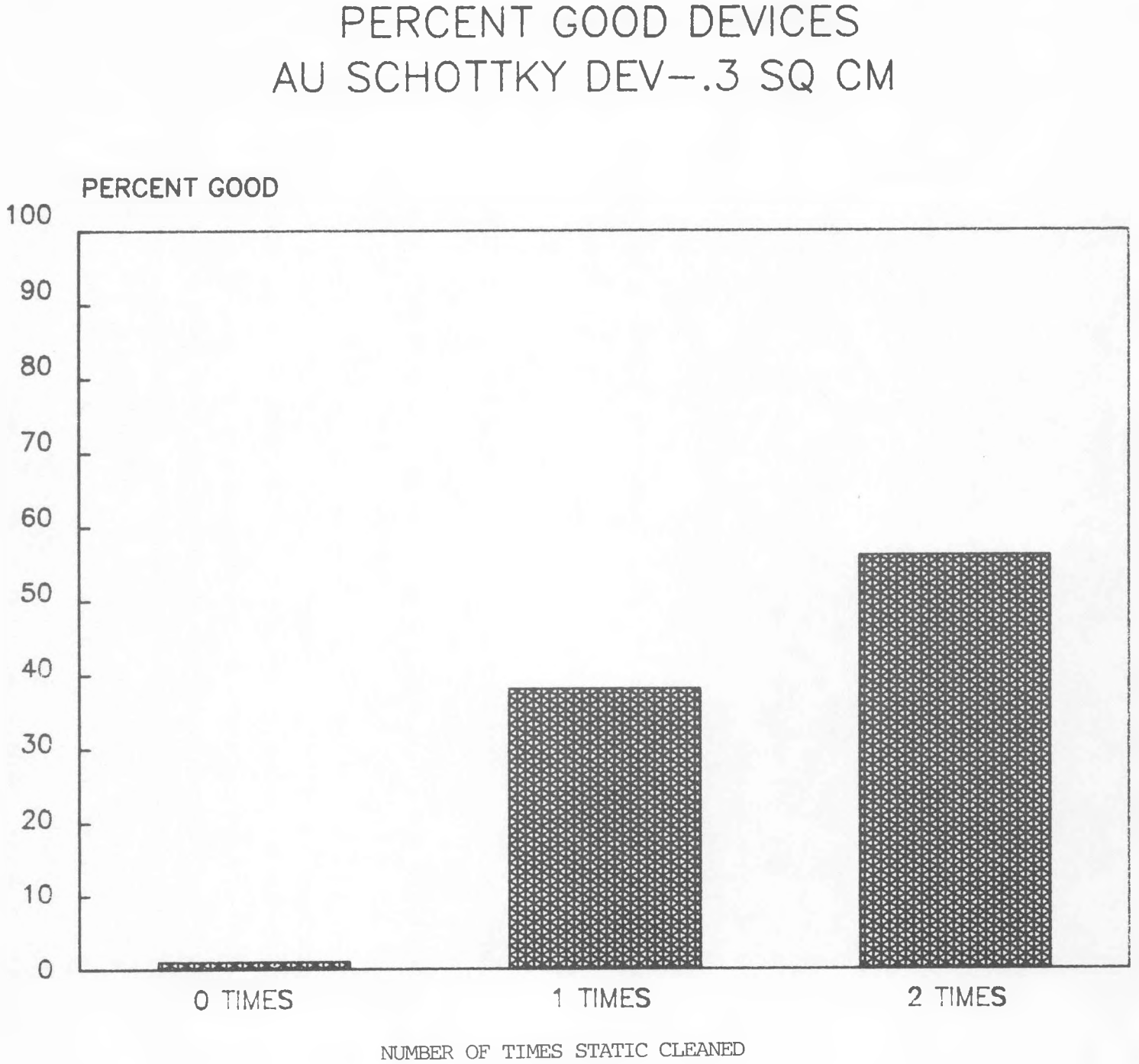

Figure 4-7. Effect Of Cleaning Procedures On The Percentage Of Good PV Devices

This experiment was performed prior to incorporating more stringent cleaning and handling methods into the device fabrication process, and demonstrates the need for such special procedures. Presently, all substrate material is handled in tightly wound rolls which are unwound only in a vacuum or in a glovebox with a nitrogen purge.

One important area which remains to be examined is the effect of polyimide substrate surface roughness on the charge collection efficiency of a-Si cells. An experiment has been initiated to analyze polyimide substrates of various defect density levels. The defect densities are determined by a method utilizing light scattering and EBIC, high magnification SEM, current-voltage, and laser scanning analysis.

Results obtained thus far indicate that even with an initial defect density much higher than glass, polyimide can be used as a flexible substrate provided that proper cleaning and handling procedures are followed. Future efforts will include completion of the substrate roughness study, followed by the initiation of studies pertaining to the relationship between high-quality device yield versus device area.

4.2 P-I-N Device Fabrication in Systems Three and Four

Studies in progress in deposition Systems Three and Four have involved three separate areas of research: 1) Substrate Effects in which devices with several different metallization layer types were fabricated on polyimide substrate from two different vendors, 2) Doping Effects in which intrinsic layer doping was performed with up to 5 ppm diborane, and 3) The Effect of Geometry on Powdering in which System Four was modified in order to decrease the occurrence of powdering during deposition.

4.2.1 Substrate Effects

Series of devices have been fabricated on polyimide substrate material obtained from two different vendors we refer to as Vendor A and Vendor B. Vendor A polyimide exhibits severe stress curling after silicon deposition. This curling problem is virtually nonexistent with Vendor B polyimide. In addition, the polyimide from Vendor B has a smoother surface topography. To date no increase in device yield has been observed. This suggests that device yield is now limited by foreign particulate contamination.

Ni, Mo, and Al metallizations all yielded high percentages of shunt-free devices on polyimide substrate from both vendors. Devices made on Al/polyimide showed very low fill factors, indicating a severe problem with the Al/a-Si interface. Two different metallization layers were evaluated for use as a diffusion barrier between the Al/a-Si interface. One of the barriers examined was (1/4 wavelength thickness) SnO_2 and the other was stainless steel (200, 100, 50, and 25 Å layer thicknesses), deposited on the Al. Details of these results are given in Section 3.0 of this report. In summary, a 1/4 wavelength thick layer of SnO_2 was not an effective barrier, whereas stainless steel barriers as thin as 25 Å, yielded devices with fill factors above 0.60.

4.2.2 Doping Effects

A dopant gas line was added to Systems Three and Four to permit compensational doping of the intrinsic layers with up to 5 ppm diborane. Devices were fabricated with intrinsic layers doped at levels of 0.1, 0.3, 1.0 and 3.0 ppm (ratio of B_2H_6 to SiH_4 flow rate) and intrinsic layer thicknesses ranging from 0.4 to 0.9 micrometer. Doping in the range of 0.3 to 3 ppm slightly increased the fill factor of the thicker devices (1 to 3% increase), but no improvement was observed in the thinner devices (0.4 micrometer intrinsic layer). It is probable that this result is due to the heavy boron carry-over from the deposition of the p^+ layer--the first deposited layer of the device.

To obtain a quantitative understanding of the boron carry-over, the photoconductance values of doped intrinsic layers on uncoated polyimide were compared to those of a nominally "undoped" intrinsic layer. The latter was deposited immediately following deposition of a p^+ layer on a previous frame of the polyimide web. Thus, the "undoped" intrinsic layer was deposited on fresh uncoated polyimide, but immediately following a typical p^+ layer deposition in the chamber.

The results show dramatic differences between the doped and "undoped" samples. In all of the doped samples without boron carry-over present, photoconductance values were approximately four orders of magnitude higher than those for dark conductance. Typical values were 10^{-7} and 10^{-11} respectively. The nominally undoped sample with boron carry-over gave light and dark conductances of 1.0×10^{-6} and 1.8×10^{-8} respectively. We conclude that boron doping cannot be effectively accomplished in our single chamber systems with a p^+-i-n^+ deposition sequence.

4.2.3 Effect of Geometry on Powdering

The severe powdering problem in System Four was eliminated by lowering the RF electrode-to-substrate gap spacing from 1 5/16" to 7/8". Spacings of 1 5/16, 1 1/16, 15/16, 7/8 and 3/4" were evaluated at a deposition pressure of 1.0 torr. The powder formation decreased significantly with decreasing distance between the showerhead electrode. At a spacing of 3/4", deposition uniformity suffered, thus the spacing was reset to 7/8". Uniformity can be improved with carefully constructed shields which give the proper gas flow pattern, but not with the flexible stainless steel sheet metal currently being used.

With the present geometry of System Four, a smooth continuous 1-meter a-SiH deposition, or up to 10 separate depositions on 4-inch frames can be obtained.

4.3 Two Chamber System

For the single deposition zone chambers used in previous work, dopant carry-over from the n^+ and p^+ layers into the intrinsic layer was common. As discussed in Section 3.2, an intrinsic layer deposited after a p^+ layer has as much boron in it as if the gas mixture had had 20 ppm of diborane. This cross contamination is believed to have an appreciable effect in reducing the fill factor of our devices. A multiple deposition chamber system is required to control this problem.

A two chamber system (System Five) was designed and made operational. The substrate passes from a feed roll through conductance limiting slits between the deposition chambers, and finally onto a take-up roll. The conductance limiting slits, through which the web enters and leaves each deposition chamber, prevent back diffusion of impurities into the deposition zones. During operation the pressure in the deposition chambers is held at 1 torr while the pressure outside the slits is 100 to 200 millitorr. Using data that was generated from the back diffusion studies, contaminants in the deposition zone should be five orders of magnitude less than the contamination level outside the deposition zone.

In System Five the fabrication of a device begins with a hydrogen etch of the substrate in the doped layer chamber followed by the deposition of a p^+ layer. The web is then wound forward to locate the proper substrate length into the intrinsic layer deposition chamber where a 5000 Å thick intrinsic layer is deposited. Finally, the web is wound backwards so that the device area is once again in the doped layer chamber where the n^+ top layer is deposited.

Figures 4-8a and 4-8b show SIMS depth profiles of a device made in a single chamber system and of one made in the new two-chamber system, respectively. The curves show the boron, phosphorous, oxygen, carbon, and nitrogen profiles for the devices. The key feature is the boron level within the intrinsic layer. As expected, the drop-off is much more abrupt for the two-chamber system than for the single chamber system.

System Five will be used exclusively to develop devices. Boron composition studies will be performed to allow efficiency and stability characteristics to be evaluated. The design of the small deposition chambers is similar to that used in the Task Five multi-chamber deposition system. Different internal geometries will be evaluated as design candidates for application in the larger system presently being built. Deposition conditions developed in the two-chamber system will also be used in initial depositions performed in the multi-chamber system.

One of special design features in System 5 which is an improvement over the other single chamber systems is the incorporation of removable mandrels for holding the substrate web. These mandrels are interchangeable with those used in the metallization system. As discussed in Section 3.1, dust attracted to the web is the prime source of shunt defects. By using interchangeable mandrels, transfer steps are eliminated, thus ensuring that the web surfaces are only exposed when in a vacuum system or a dust-free glovebox. This process greatly reduces the possibility of dust particles contacting the web and this should reduce defects in the devices.

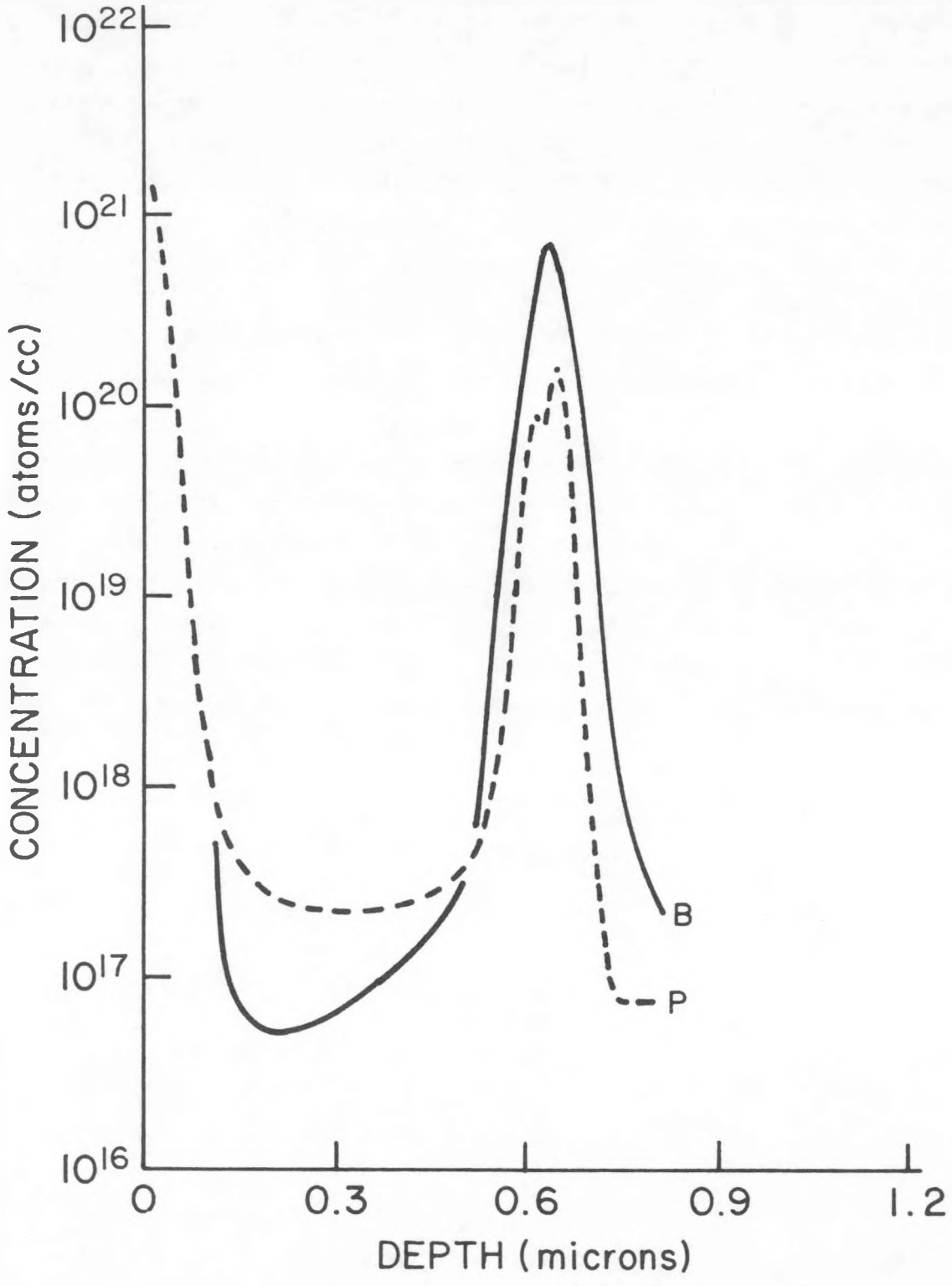

Figure 4-8. (a) SIMS Depth Profile Of Device Made In Single Chamber System

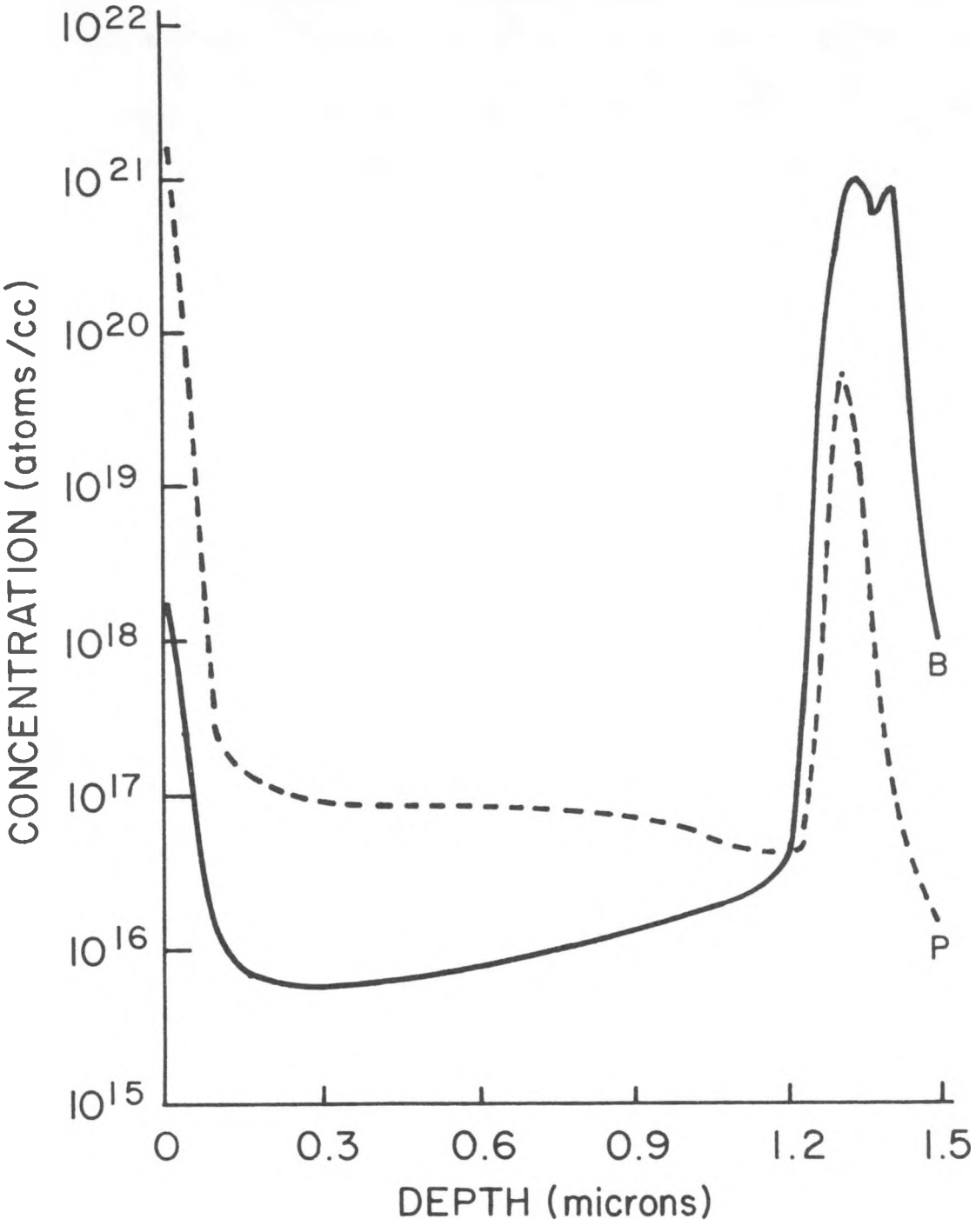

Figure 4-8. (b) SIMS Depth Profile Of Device Made In Two-Chamber System

4.4 Device Stability

In earlier device fabrication efforts using continuous ITO deposition difficulty in producing stable devices was encountered. Severe declines in device fill factors were observed. A critical parameter in this degradation process was exposure to air since the series resistance increased due to the ITO. Details of the investigation relating to the ITO problem are discussed in Section 4.2. Improvements have subsequently been made in the ITO coating process that allow the fabrication of devices having improved stability.

5.0 TASK FOUR - MONOLITHIC, INTRA-CONNECTED CELLS/SUBMODULE RESEARCH

5.1 Series Connected Submodule Design

A common problem in all solar cells is the electrical power loss due to the series resistance of the cell. A major contributor to this series loss results from the cell's front transparent electrode. The traditional approach used to control this loss is to deposit a conductive grid structure on the front surface. Drawbacks associated with grid structures include complexity of design and construction as well as loss in active area of the device. Disadvantages such as these can be minimized by employing the monolithic, series connected submodule structure [5] shown in Figure 5-1.

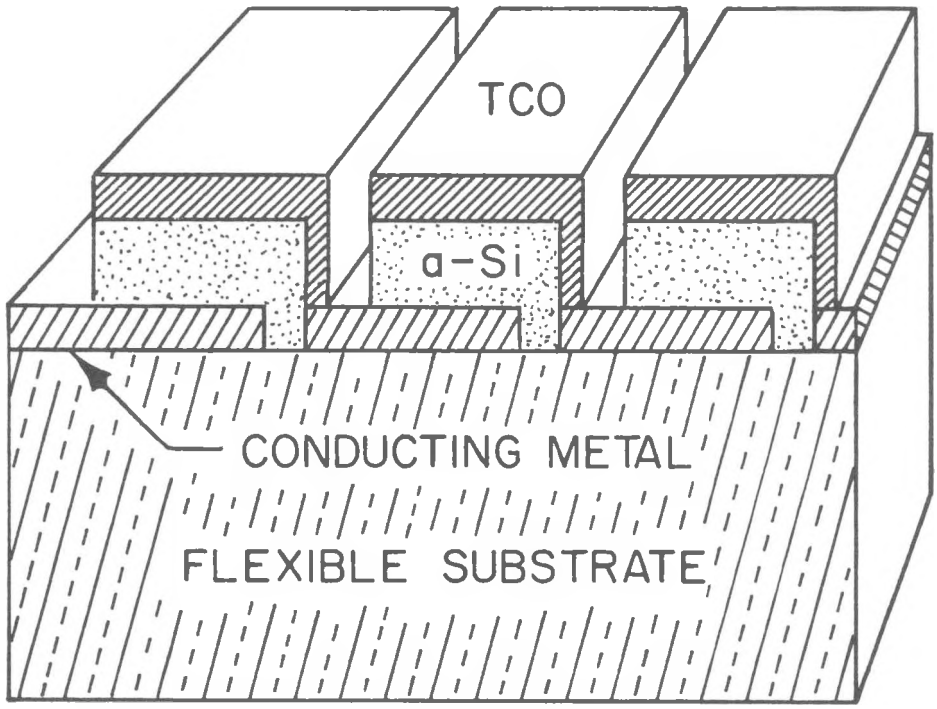

Figure 5-1. **Submodule Design Concept**
TCO refers to Transparent Conductive Oxide

The submodule design shown in Figure 5-1 is the preferred type of structure for large area flat arrays. The dimensions to be used in the finished device can be estimated from the materials properties. The parameter of greatest concern is the overall efficiency of the finished submodule. The resultant efficiency can be calculated assuming the losses are due only to ohmic losses in the top and bottom conductive layers [5, 6, 7, 8, 9]. The result is:

$$E = [e-(1/3)(R/P)J^2(W-S)^2]\ [1-S/W] \qquad \text{(Eq. 5-1.)}$$

where:

E = overall efficiency of the submodule

R = sum of the sheet resistances of the conductive layers

e = small area active device efficiency

P = incident power per unit area from the light source

J = current output per unit area of active cell

W = width between the scribe lines

S = width of the individual scribe regions (scribe width)

Figures 5-2 and 5-3 illustrate this function under various conditions. Note that decreased efficiencies at small W are due to losses in active area from the scribe lines while decreased efficiencies at large W are due to ohmic losses in the top contact layer. Most of the ohmic loss is due to the TCO layer since R is almost totally due to the TCO sheet resistance.

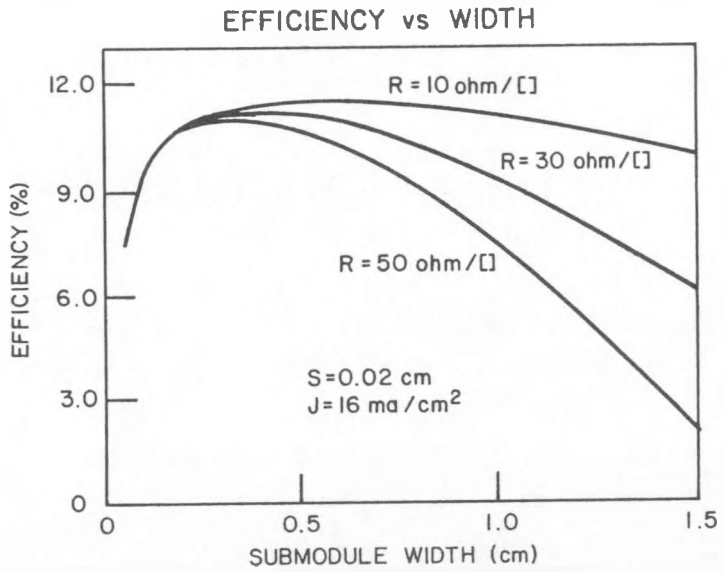

Figure 5-2. Efficiency Of The Submodule Versus Cell Width For Three Values Of Sheet Resistance Of The TCO Layer
A 12% small area efficiency for the device is assume under AM1 conditions, and J represents the short circuit current density.

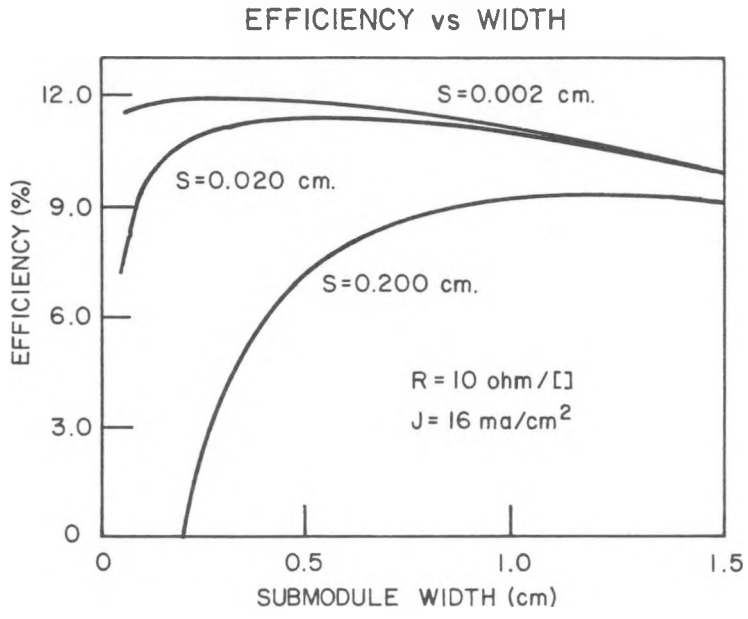

Figure 5-3. Efficiency Of The Submodule Versus Cell Width For Three Values Of The Scribe Width
A 12% small area efficiency for the device is assumed under AM1 conditions and J represents the short circuit current density.

The parameters which are expected to be used in solar cell construction have been established in order to set a baseline submodule design goal. The active web width has been established by deposition considerations. The scribe width is determined by the region of overlap between the values obtained from work involving photoresist and laser scribing [5, 7]. The sheet resistance of the transparent conductive layer is expected to improve to a value of approximately 10 ohms/square as compared to present films with a sheet resistance of 35 ohms/square at 2100 $\mathring{A}$ thickness. Values for the cell current density and the active area power production are also expected to improve to values of approximately J = 16 mA/cm^2 for a short circuit current density and P = 11.1 mW/cm^2 under AM1 conditions (a small area efficiency of 12%).

The parameters for the target submodule are given in Table 5-1:

Table 5-1. Target Submodule Parameters

web length	up to	100.00 cm
web width	=	10.00 cm
scribe width	=	0.02 cm
sheet resistance of top contact	=	10.00 ohm/[]
short circuit current density	=	16.00 mA/cm^2
small area power output (AM1)	=	11.10 mW/cm^2
cell width	=	0.50 cm

Any parameter modifications required as a result of unanticipated changes in materials properties can be accommodated by varying the submodule width.

5.2 Series Connected Submodule Construction

For the scribing operations which are required to produce the series connections in the submodules, several methods have been suggested which include mechanical masking during deposition, diamond scribing, photoresist processing with chemical or ion beam etching, and laser scribing. Diamond scribing must be ruled out because of difficulties encountered in scribing on a flexible substrate. With mechanical masking during continuous deposition, difficulty arises in producing clean, repeatable scribes and in keeping the vacuum system clean. The two techniques which appear to be the most favorable are chemical etching and laser scribing. While chemical etching is well suited to submodule prototype building, the development of laser scribing will be the ultimate approach to be utilized in future large scale production [10].

Samples for evaluation of the submodule design have been chemically etched using a commercially available photoresist process. Scribe regions of approximately 0.02 cm were obtained using this technique. This practical limit is due to the dimensional instability of the flexible substrate.

The laser scribing technique has been demonstrated with submodules on glass substrates [7, 11]. These laser processing steps are also applicable to flexible substrates. Due to potential stretching of the substrate material during processing, the laser technique can be more applicable to the registration of multiple cuts than conventional masked photoresist technology.

Figure 5-4a and b illustrate two methods of making the series connections. In Figure 5-4a the traditional method used with photoresist processing is shown. In Figure 5-4b the most suitable method for laser scribing is illustrated [11]. Figure 5-5 shows three scanning electron microscope (SEM) photographs of initial laser scribe results. Figure 5-6 shows optical micrographs of YAG laser cuts for each of the three scribe types.

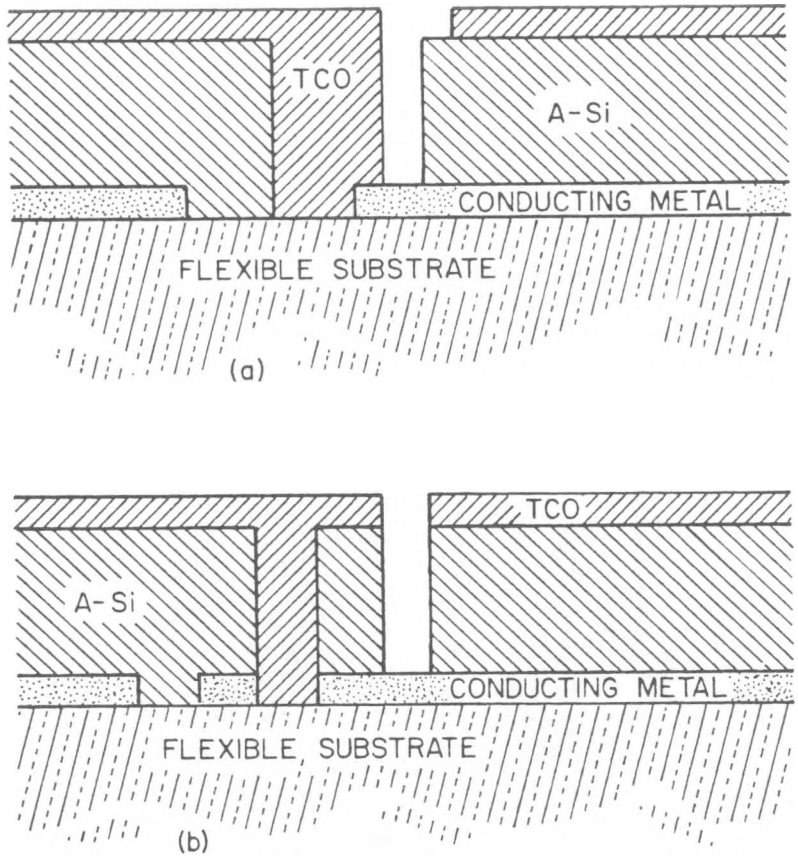

Figure 5-4. Submodule Interconnect Region: (a) For Photoresist Work, (b) For Laser Scribing

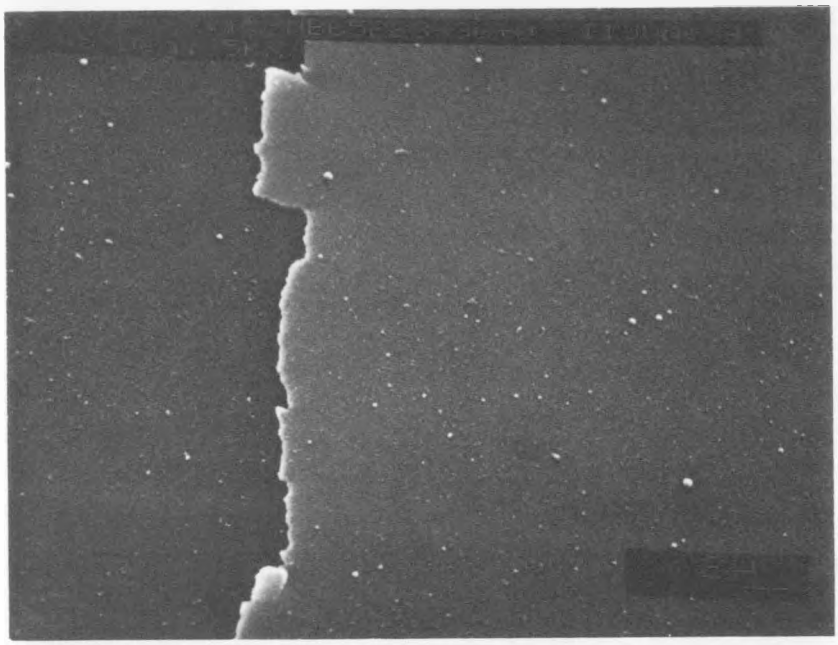

Figure 5-5. SEM Photos Of Laser Scribed Materials

(a) Scribed stainless steel on polyimide.

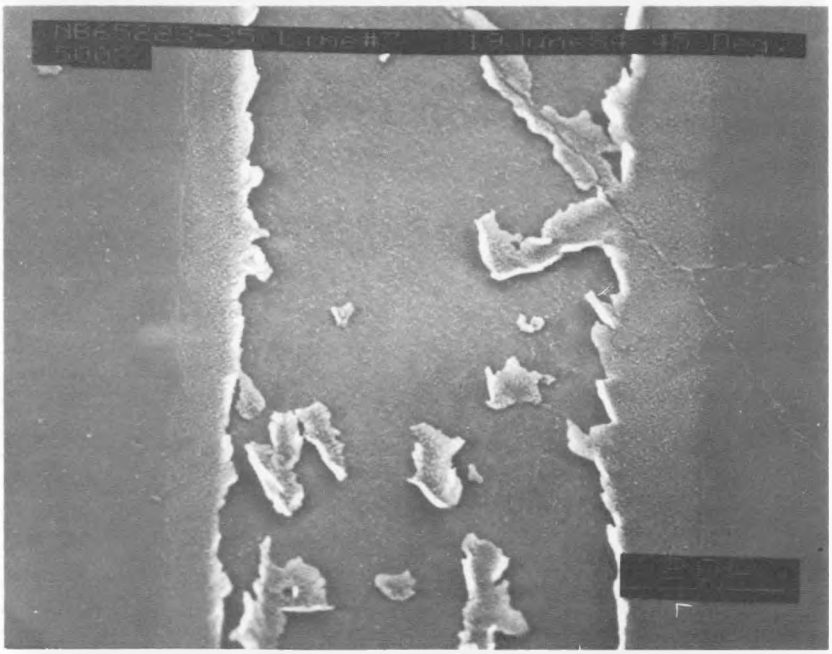

(b) Scribed amorphous silicon on stainless steel.

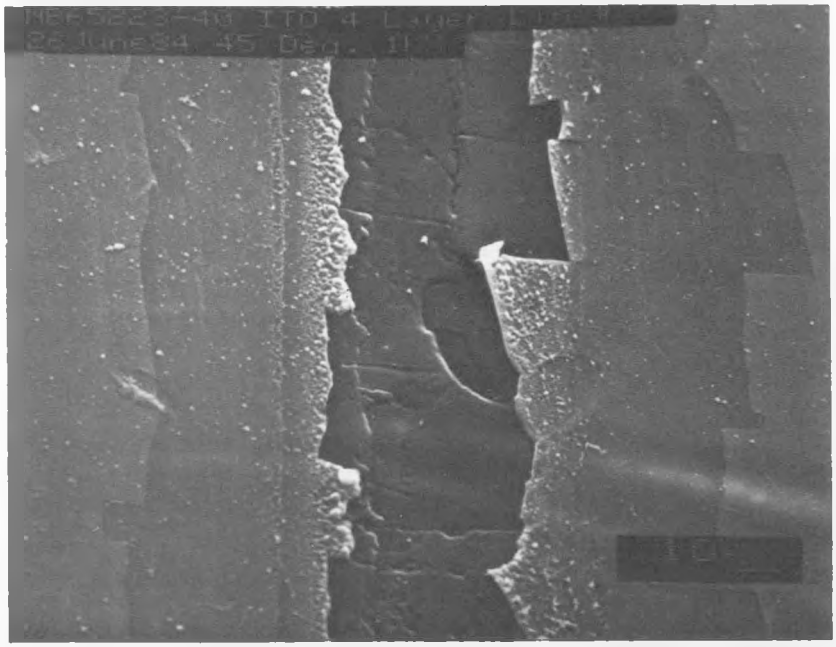

(c) Scribed ITO on amorphous silicon on stainless steel on polyimide.

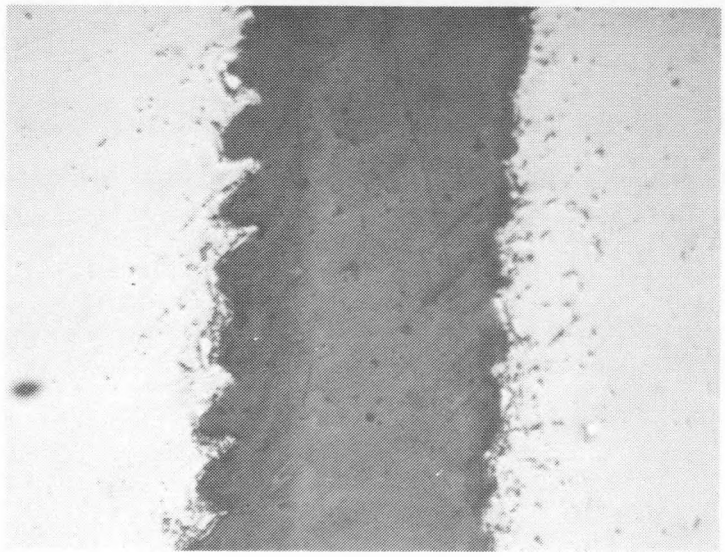

Figure 5-6. Optical Micrographs Of YAG Laser Cuts

(a) Scribed Ni on polyimide

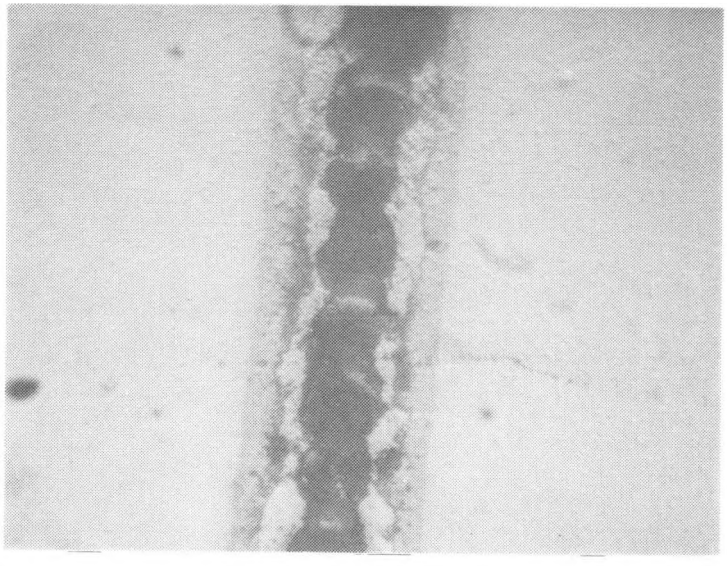

(b) Scribed a-Si on Ni

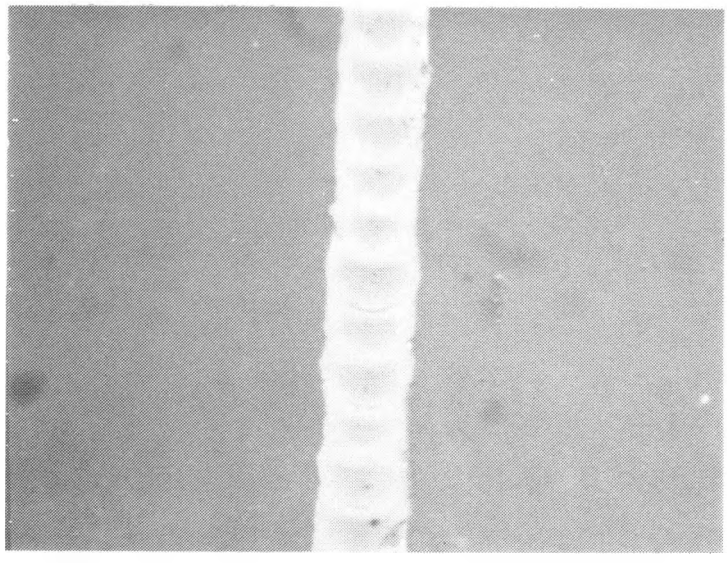

(c) Scribed ITO on a-Si

The equipment used to laser scribe the submodules is shown in Figure 5-7. The He-Ne laser and photodetector are used to sense the position of the first scribe in the metal layer for indexing the second and third cuts. This equipment has been used with both Argon and YAG lasers. Presently, the 532 nm frequency doubled YAG laser line is the preferred wavelength for scribing all three layers of material in our solar cells. Below 532 nm, the polyimide becomes very absorptive and is damaged by the laser radiation. Figure 5-8 shows an optical transmission curve for polyimide which reinforces the advantage of using the YAG laser.

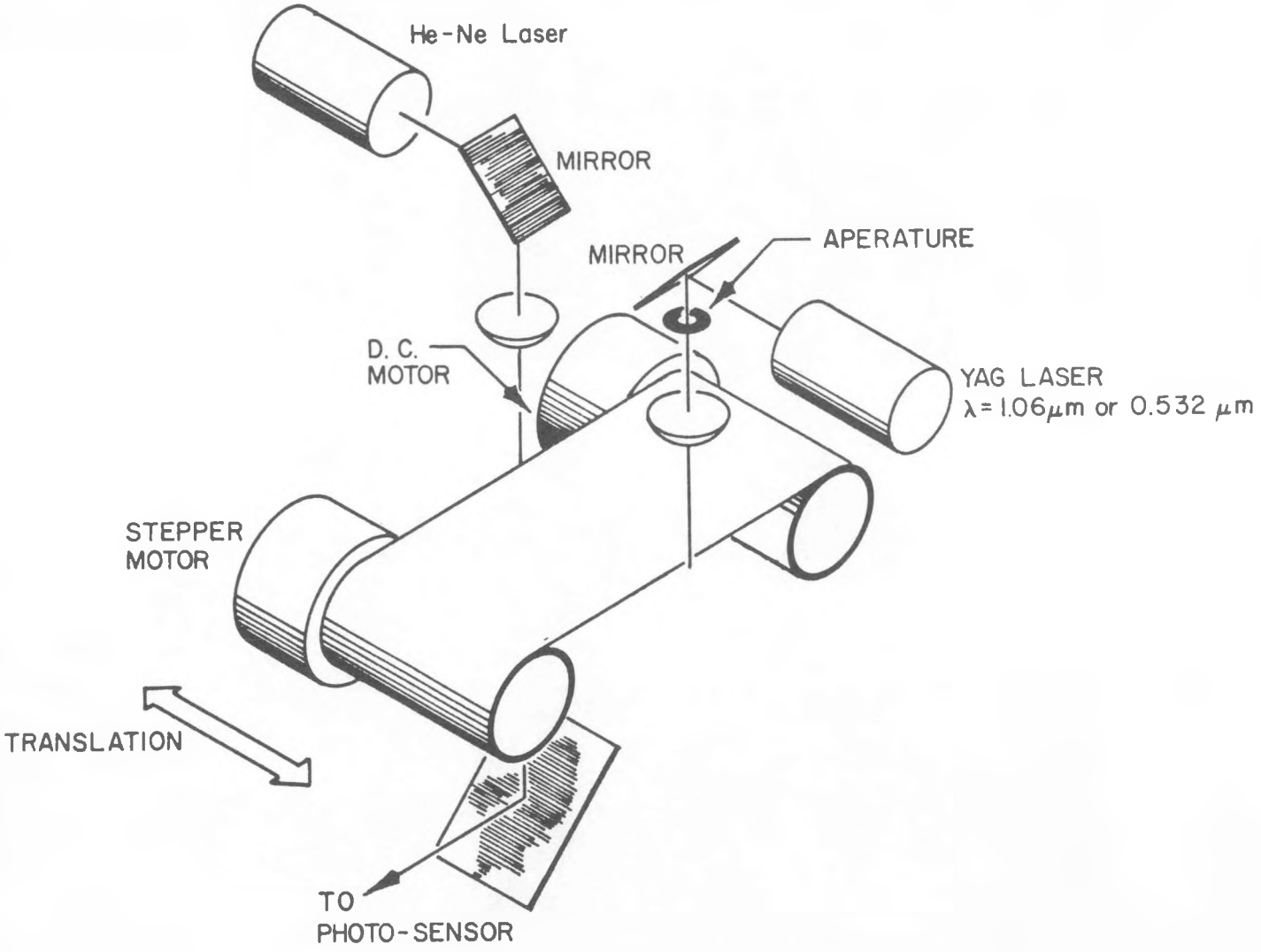

Figure 5-7. Equipment Used To Laser Scribe Submodules

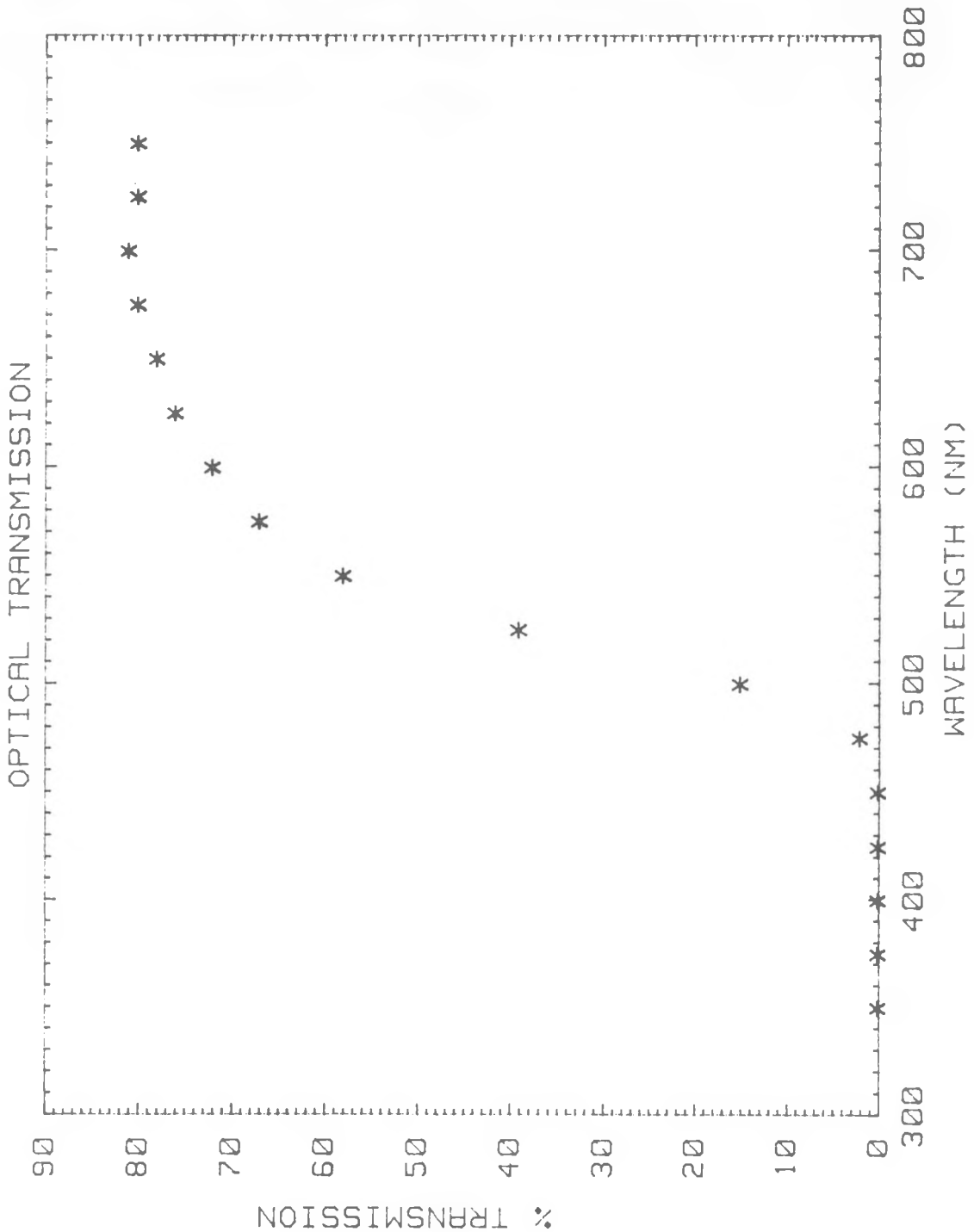

Figure 5-8. Optical Transmission Of Polyimide

5.3 Solar Simulation

A major goal of this project is to produce submodules of area greater than 1000 cm^2 with an efficiency of greater than 8%. Two laboratory-based solar simulator systems are available for monitoring progress in meeting this efficiency goal. One of the systems, a small solar simulator consisting of a single ELH bulb light source, has been used to report results in Task 3. The other system is a large area (10 cm x 10 cm), 5 bulb ELH solar simulator which was constructed by the Institute of Energy Conversion at the University of Delaware. Representative output data from this system is shown in Figure 5-9. Calibration of the solar simulators is accomplished by a combination of measurements using radiometers, and standard single crystal cells, both with and without wavelength filters. Two distributors of stable single crystal solar cells are Applied Solar Energy Corporation (ASEC) and Hamamatsu Corporation [12].

HAM-1 - 3 3-APR-85 TEST # 1003
AREA= 0.660E-01sqcm .00 hr 0 deg C

VOC	JSC	VMP	JMP	RESVOC		GOOD
.5152	10.05	.3964	9.248	7.94	28.3 deg C	A fact.=1.000
.0014	0.0000E+00	.0021	0.5379E-01		87.50 mW/sqcm	CALIB

FF	EFF	R	G	JL	J0	# PTS	# ITER	ERROR
70.83	4.19	5.338	.290	10.06	2.418E-08	363	4	0

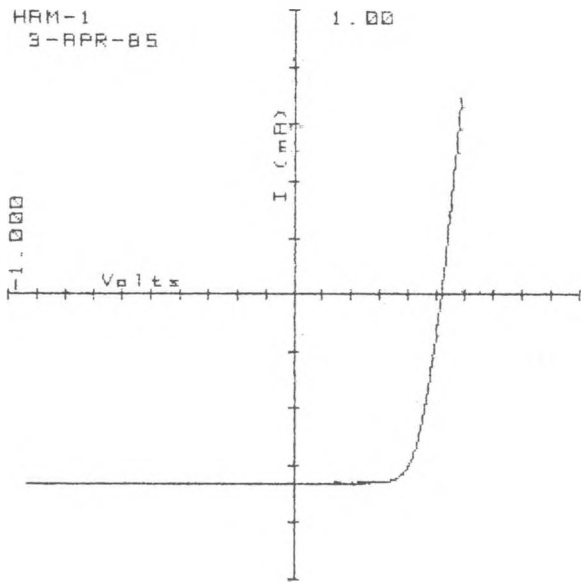

Figure 5-9. Large Area Solar Simulator Output For A Hamamatsu S1133 Photodiode

5.4 Laser Scanning

A laser scanner with a line scan output will be used to evaluate the submodules and to detect small area defects [13, 14]. The scanner uses a He-Ne laser as the light source with the beam focused to a 100 micron diameter spot. Results from laser scanning and EBIC are used to provide early indications of defect types and the defect density in the submodules. This information will be utilized in improving the deposition and materials properties of the Transparent Conductive Oxide and a-Si layers. Furthermore, it will be useful in designing methods to subdivide the submodule to minimize the effects of defects [15].

Several excellent reviews addressing the field of laser scanning have been published [16-20]. An examination of alternatives indicates the most cost effective method for scanning up to 4 inches by 4 inches (100 cm^2) solar cells for defects is to use a simple x-y translation stage as shown in Figure 5-10.

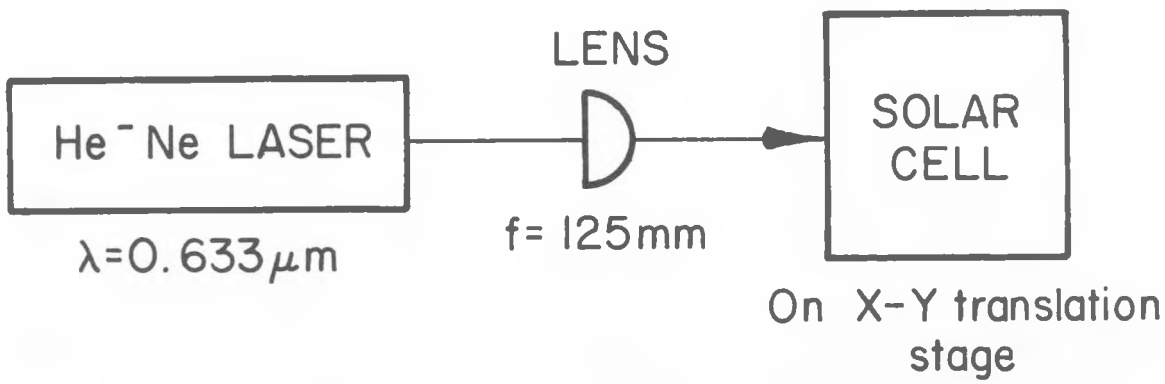

Figure 5-10. Laser Scanned System Configuration

The equations that describe the optics when using Gaussian laser beams are:

$$\Theta_o \, d_o = \frac{4\lambda}{\pi} \qquad \text{(Eq. 5-2a)}$$

$$d_o' = \frac{4\lambda}{\pi} \, \frac{f}{d_o} \qquad \text{(Eq. 5-2b)}$$

$$Z_R = \pm \frac{\pi}{4\lambda} \, d_o^2 \qquad \text{(Eq. 5-2c)}$$

where: Θ_o is the beam divergence angle
d_o is the beam waist
d_o' is the beam waist on the output side of a lens
λ is the laser wavelength
f is the lens focal length, and
Z_R is a measure of the depth of focus known as the Rayleigh Range

Note that $\Theta_o d_o$ is a constant for a given wavelength. For a HeNe laser, $\lambda = 0.633$ micrometer, so, $4\lambda/\pi = 0.8$ micrometer. Equation 5-2b can be used to calculate the focal length since most commercial He-Ne lasers have d_o approximately equal to 1 millimeter. This yields a value for f of approximately 125 millimeters for a spot size equal to 100 micrometers at the solar cell. Equation 5-2c yields a depth of focus of $\pm$ 1.24 centimeters.

The utility of the laser scanner system, shown in Figure 5-10 can be expanded by adding a roll-to-roll web feed stage to the x-y translation stage so that a 10 centimeter wide by 100 centimeter long web can be scanned. An interface to an x-y pen recorder allows two-dimensional representations of the solar cell response to the laser scan as shown in Figure 5-11. Figure 5-12, shows laser scanner output produced by Pat Lasswell at the Institute of Energy Conversion located at the University of Delaware.

Figure 5-11. Short Circuit Current Profile

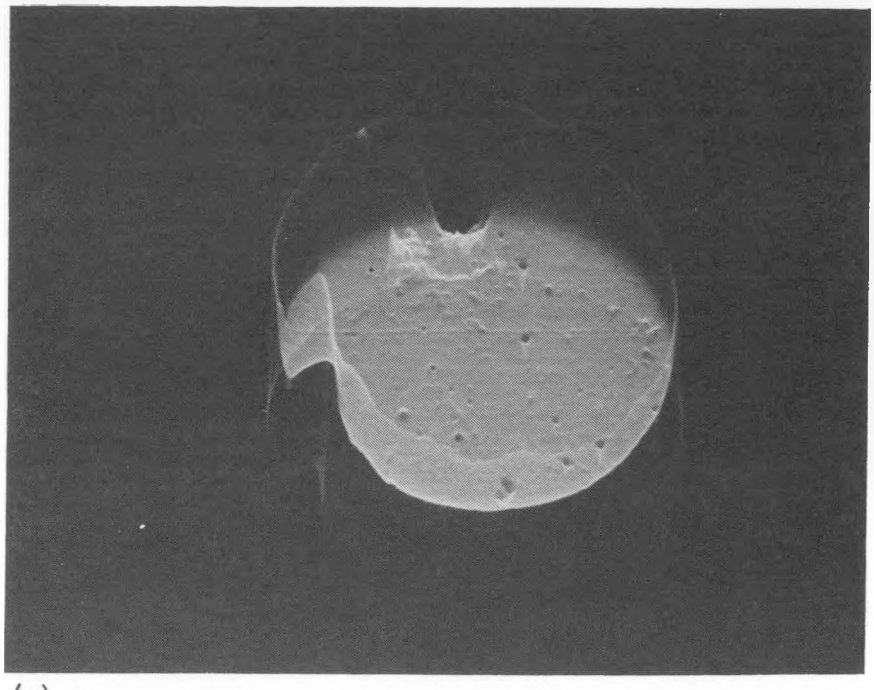

(a)

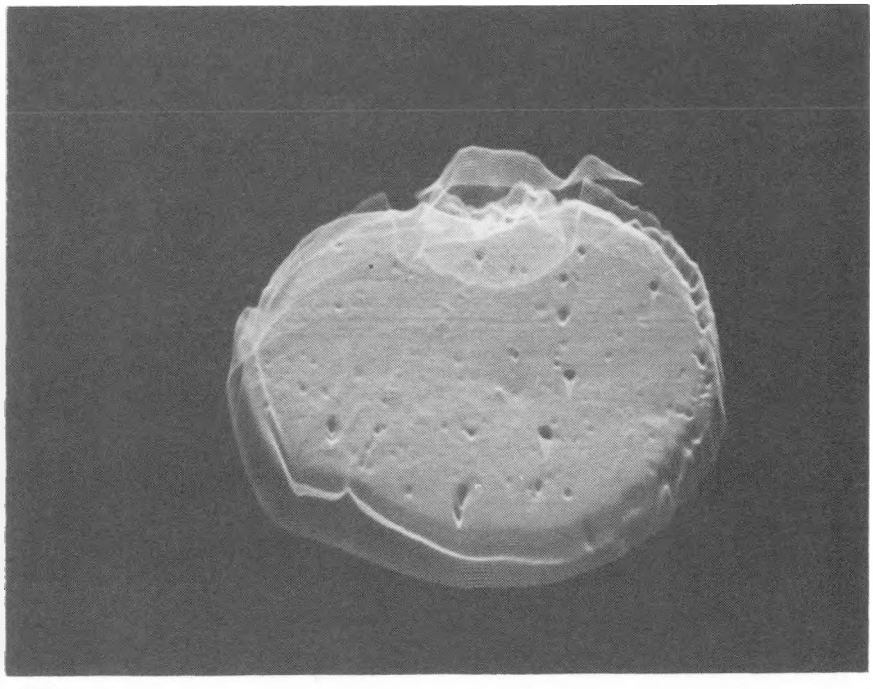

(b)

Figure 5-12. Laser Scanned Solar Cells
(a) 5 Square Millimeter Chrome Dot Evaporated Near The Middle Of The Substrate
(b) 5 Square Millimeter ITO Dot Deposited Near The Chrome Dot Scanned In Figure 5-7 (a)

6.0 TASK FIVE - MULTI-CHAMBER DEPOSITION SYSTEM

Work during this semester has concentrated on the construction of the multi-chamber deposition system. This system will be used in future work to deposit a-Si p-i-n layers onto flexible polyimide web in a sequential and continuous process without breaking vacuum. The system design is expected to provide very low cross-contamination between deposition zones. The level of cross-contamination in the intrinsic deposition zone is expected to be less than 1 ppm. This low level is necessary because the properties of intrinsic films are very sensitive to the dopant gases used in the n and p deposition zones. Dopant levels in the n and p zones usually range between 0.5 and 2%.

Assembly of the multi-chamber deposition system is approximately 90% complete. The system has been helium leak-checked and a base pressure of 1×10^{-6} torr has been achieved during initial testing. Six gas purge units purchased from Veriflo Corporation have been installed in gas cabinets, and process gas cylinders are in place. Gas cylinders have been previously analyzed by our modulated beam gas analysis system and all gases appear to be sufficiently pure. A gas manifold system that contains 15 Tylan mass flow controllers is presently being assembled by Perkin-Elmer Vacuum Products. VCR fittings are used exclusively in the entire gas handling system in order to maintain clean and leak-tight operation. All components will be helium leak-checked just prior to introducing process gas into the gas manifold.

In view of the hazards to personnel when using silane, phosphine, and diborane, an MDA toxic gas detector was purchased and will soon be installed in the laboratory. The unit has eight channels for gas detection; three will be used on the multi-chamber. The unit will be connected to the multi-chamber safety circuit with both visual and audible alarms. In the event of a toxic gas leak, all gas flow to the multi-chamber is automatically shut off. Similarly, process gas is shut off in the event of power failure, loss of exhaust ventilation, loss of nitrogen purge gas, or abnormally high system pressure. One additional safety measure taken was to locate the process pump and process gases in a separate room away from the multi-

chamber. Personnel will not be in this room except when changing gas cylinders or servicing the process pump. A self-contained breathing apparatus is also conveniently located in the laboratory in the event of a major gas spill.

The multi-chamber deposition system is expected to become fully operational by May 31, 1985. Major items yet to be completed are the installation of the gas manifold assembly, installation of exhaust ducts for the process pumps and gas cabinets, and installation of the MDA gas detector.

7.0 REFERENCES

1. Moore, A.R., Appl. Phys. Lett., 40 (5), March 1, 1982, pp. 403-405.

2. Moore, A.R., SEMICONDUCTORS AND SEMIMETALS, VOL. 21, PART C, Academic Press, Inc., 1984, pp. 239-256.

3. Patel, R.I., "Thermodynamic Study of the Silane-Hydrogen Chemical System," Proceedings of the Materials Research Society, April, 1985.

4. As reported at PVSEC-1, November 13-16, 1984, Kobe, Japan.

5. Hanak, J.J., "Monolithic Solar Cell Panel of Amorphous Silicon," Solar Energy, Vol. 23, 1979, p. 145.

6. Wyeth, N. Convers, "Sheet Resistance Component of Series Resistance in a Solar Cell as a Function of Grid Geometry," Solid State Electronics, Vol. 20, 1977, p. 629.

7. Tyan, Y. and E.A. Perez-Albuerne, "A Simple Monolithically Integrated Thin-Film Solar Cell Array," Record of the 16th IEEE Photovoltaic Specialists' Conference, 1982, p. 928.

8. Kiss, Z., "Research on High Efficiency Single-Junction Monolithic Thin Film Amorphous Silicon Solar Cells," SERI Amorphous Silicon Subcontractors Review Meeting, December, 1983.

9. Gupta, Y., H. Liers, S. Woods, S. Young, R. DeBlasio, and L. Mrig, "Optimization of a-Si Solar Cell Current Collection," Record of the 16th IEEE Photovoltaic Specialists' Conference, 1982, p. 1092.

10. Firester, A.H., "The Manufacture of Amorphous Silicon Photovoltaic Modules, Proceedings of the SPIE - Photovoltaics for Solar Energy Applications II, Vol. 407, 1983, p. 37.

11. Yamazaki, S., K. Itoh, S. Watabe, A. Mase, K. Urata, K. Shibata and H. Shinohara, "Mask-less Fabrication of a-Si Solar Cells Using Laser Scribe Process," Record of the 17th IEEE Photovoltaics Specialists' Conference, 1984.

12. Applied Solar Energy Corporation, 15251 E. Don Julian Road, City of Industry, California, (213) 968-6581.

13. Takakura, H., K. Fujimoto, K. Okuda, C. Coluzza and Y. Hamakawa, "Spectroscopic Laser Scanning Analysis of Photo-Induced Current on a-Si Solar Cells," Japanese Journal of Applied Physics, Vol. 22, 1983, p. 569.

14. SERI Photovoltaic Advanced Research and Development: An Overview, SERI/sp-281-2235, February, 1984, DE84004492, U.C. Category 63. Available from: Superintendent of Documents, U.S. Government Printing Office, Washington, D.C. 20402.

15. Tyan, Y. and E.A. Perez-Albuerne, "A Simple Scheme for the Minimization of the Impact of Shorting Defects in Large Area Thin Film Integrated Arrays," Record of the 17th IEEE Photovoltaics Specialists' Conference, 1984.

16. Hopkins, R.E., and M.J. Buzawa, "Optics For Laser Scanning, "Optical Engineering, Vol. 5 #2, 1976, p. 90.

17. Berg. A.D., "Optical Design Problems in Laser Scanning and Reading Systems," Vol 69 - Optical Design Probelms in Laser Systems (SPIE), 1975, p. 14.

18. Westcott, M., "Sorting out the Scan Lens Puzzle," Photonics Spectra, May, 1984, p. 91.

19. Beiser, L., "Laser Scanning Systems," Laser Applications Vol. 2, 1974, p. 53.

20. Starkweather, G.K., "High Speed Laser Printing Systems," Laser Applications, Vol. 4, 1980, p. 125.